



Tectonics

RESEARCH ARTICLE

10.1002/2016TC004211

Key Points:

- New framework for using AHe thermochronology to investigate the lateral growth of faults
- Rapid exhumation onset ages along strike are uniform within error on the Pine Forest Range normal fault in Nevada
- Results are most consistent with a constant fault-length model for fault growth

Supporting Information:

- Supporting Information S1
- Table S1

Correspondence to:

M. A. E. Curry,
maggellis@gmail.com

Citation:

Curry, M. A. E., J. B. Barnes, and J. P. Colgan (2016), Testing fault growth models with low-temperature thermochronology in the northwest Basin and Range, USA, *Tectonics*, 35, doi:10.1002/2016TC004211.

Received 18 APR 2016

Accepted 20 SEP 2016

Accepted article online 24 SEP 2016

Testing fault growth models with low-temperature thermochronology in the northwest Basin and Range, USA

Magdalena A. E. Curry^{1,2}, Jason B. Barnes^{1,3}, and Joseph P. Colgan⁴

¹Department of Geological Sciences, University of North Carolina at Chapel Hill, Chapel Hill, North Carolina, USA, ²Now at Jackson School of Geosciences, University of Texas at Austin, Austin, Texas, USA, ³Now at Landscape Analytics LLC, Seattle, Washington, USA, ⁴U.S. Geological Survey, Lakewood, Colorado, USA

Abstract Common fault growth models diverge in predicting how faults accumulate displacement and lengthen through time. A paucity of field-based data documenting the lateral component of fault growth hinders our ability to test these models and fully understand how natural fault systems evolve. Here we outline a framework for using apatite (U-Th)/He thermochronology (AHe) to quantify the along-strike growth of faults. To test our framework, we first use a transect in the normal fault-bounded Jackson Mountains in the Nevada Basin and Range Province, then apply the new framework to the adjacent Pine Forest Range. We combine new and existing cross sections with 18 new and 16 existing AHe cooling ages to determine the spatiotemporal variability in footwall exhumation and evaluate models for fault growth. Three age-elevation transects in the Pine Forest Range show that rapid exhumation began along the range-front fault between approximately 15 and 11 Ma at rates of 0.2–0.4 km/Myr, ultimately exhuming approximately 1.5–5 km. The ages of rapid exhumation identified at each transect lie within data uncertainty, indicating concomitant onset of faulting along strike. We show that even in the case of growth by fault-segment linkage, the fault would achieve its modern length within 3–4 Myr of onset. Comparison with the Jackson Mountains highlights the inadequacies of spatially limited sampling. A constant fault-length growth model is the best explanation for our thermochronology results. We advocate that low-temperature thermochronology can be further utilized to better understand and quantify fault growth with broader implications for seismic hazard assessments and the coevolution of faulting and topography.

1. Introduction

Faults grow by elongating and accumulating displacement. Field observations of historical earthquakes and mature fault systems show that both single-event earthquake slip and finite displacement increase proportionally with fault length (Figure 1 [Cowie and Scholz, 1992a, 1992b; Schlische *et al.*, 1996]). This observation has led to a well-established scaling relationship that is the basis for most current models of fault growth, whereby there is a simultaneous increase in displacement and fault length as a result of repeated earthquakes (Figure 2a [Gillespie *et al.*, 1992]). Many studies utilize this relationship to make inferences about fault growth based on static length and/or displacement measurements [Gillespie *et al.*, 1992; Densmore *et al.*, 2007a; Polit *et al.*, 2009; Barnes *et al.*, 2011; Davarpanah and Babaie, 2013; Nahm *et al.*, 2013]. Unfortunately, due to a paucity of observations on the lateral growth of faults along strike, our understanding of fault-system evolution beyond this idea is stalled [Morewood and Roberts, 2002]. Thus, it remains debatable whether fault displacement and length always increase concomitantly or if this displacement-length scaling only describes faults at certain periods in development [Walsh *et al.*, 2002]. For example, a growing amount of evidence suggests that some faults reach or approach their maximum length relatively early in their history, at which point further growth is achieved by displacement accumulation with little to no lengthening (Figure 2c [Morewood and Roberts, 1999; Walsh *et al.*, 2002; Childs *et al.*, 2003; Bennett *et al.*, 2006; Amos *et al.*, 2010; Mouslopoulou *et al.*, 2012]). These results appear to contradict the conventional model for fault growth that advocates concurrent displacement and elongation (compare Figures 1, 2a, and 2c), suggesting that the conventional model is not appropriate to describe fault growth in some situations.

More direct observations on the 3-D kinematics of natural fault systems are clearly needed to further test existing models of fault growth. Understanding the precision, accuracy, and predictability of these conceptual models is critical for seismic hazard applications [Nicol *et al.*, 2005; Kim *et al.*, 2011; Ascione *et al.*, 2013],

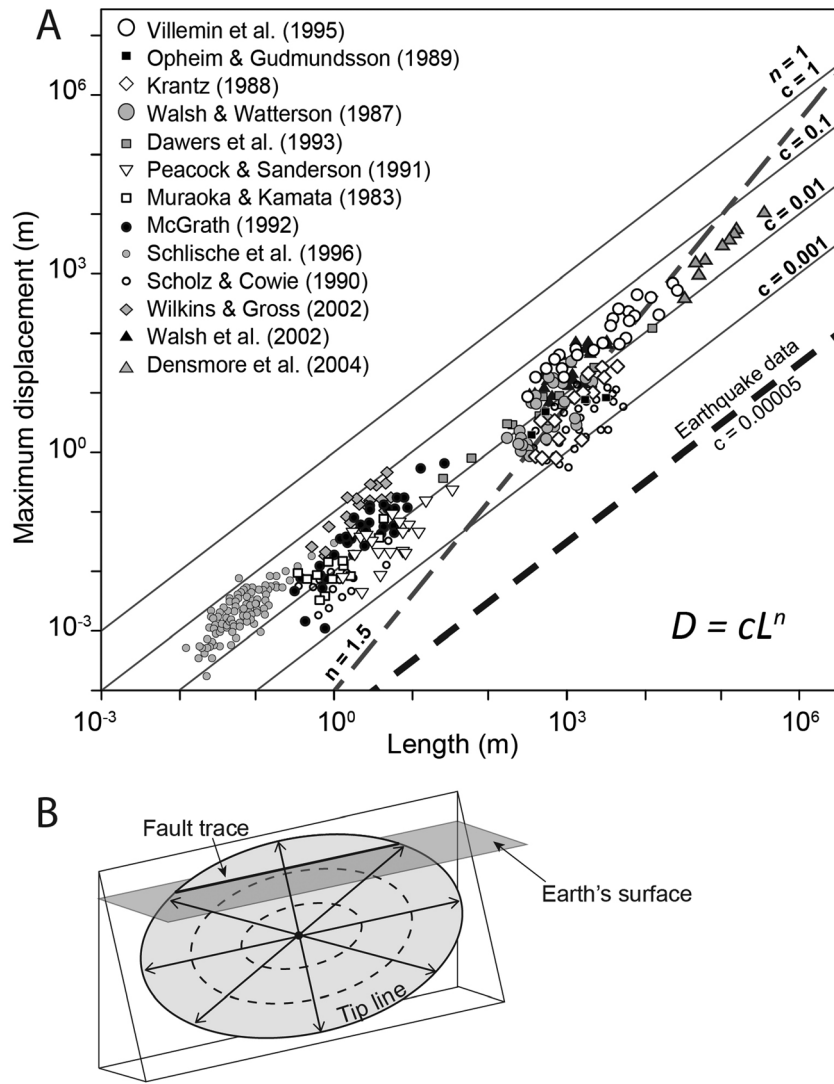


Figure 1. Basis for existing fault growth models. (a) Normal fault displacement (D) versus length (L). The average position of earthquake data for all fault types is the thick dashed line [Wells and Coppersmith, 1994]. The empirical relationship is described by $D = cL^n$, where c is a constant with values of $\sim 10^{-1} - 10^{-3}$ and n is between 1 and 1.5. (b) Idealized elliptical fault surface radially propagating toward the tip line. The dashed lines represent the increasing D and L of the fault plane through time. The measured dimensions (D, L) will vary with the fault trace at the plane of inspection (Earth's surface) [modified from Walsh et al., 2003; Kim and Sanderson, 2005]. Data sources: Villemin et al. [1995]; Opheim and Gudmundsson [1989]; Krantz [1988]; Walsh and Watterson [1987]; Dawers et al. [1993]; Peacock and Sanderson [1991]; Muraoka and Kamata [1983]; McGrath [1992]; Schlische et al. [1996]; Scholz and Cowie [1990]; Wilkins and Gross [2002]; Walsh et al. [2002]; and Densmore et al. [2004].

understanding links between faulting and landscape development [Densmore et al., 2007b; Barnes et al., 2011], and even the distribution of natural resource reservoirs of geothermal energy, hydrocarbons, and groundwater [Strachan et al., 2013; Egger et al., 2014; Jackson et al., 2014; Faulds and Hinz, 2015]. Apatite (U-Th)/He thermochronology (AHe) has been widely and successfully used to date the timing of slip on normal faults (Figure 3 [e.g., Stockli, 2005; Colgan et al., 2006a]). To our knowledge, however, this very pertinent low-temperature thermochronometer has only once been used to quantify lateral fault propagation [Krugh, 2008]. Notably, several studies have investigated lateral fault propagation in reverse fault systems [e.g., Medwedeff, 1992; Bennett et al., 2005; Sobel et al., 2006; Amos et al., 2010], but there remain few studies that document the lateral growth of normal faults using field observations [Morewood and Roberts, 1999]. We posit that AHe can be more rigorously implemented to address outstanding questions and deficiencies in our understanding of how faults evolve in space and time.

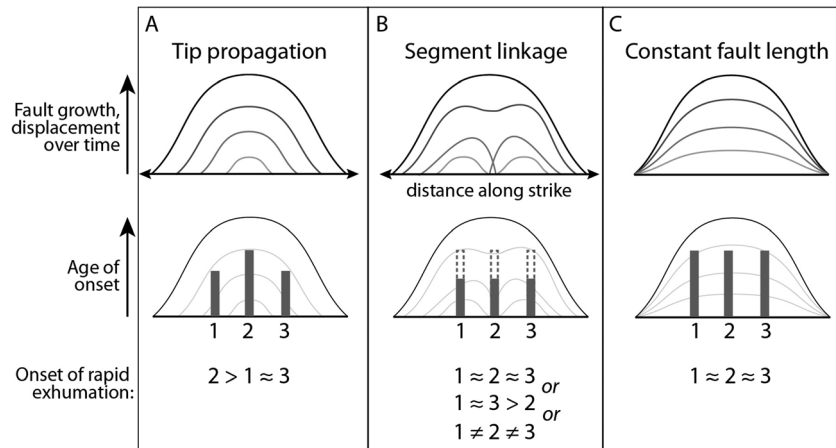


Figure 2. Schematic diagrams of fault growth models and expected onset of rapid exhumation relationships recorded by thermochronology age patterns from age-elevation profiles at various along-strike locations. Fault growth models are (a) tip propagation, (b) segment linkage, and (c) constant fault length [Nicol *et al.*, 2005]. The thick horizontal lines are the fault traces that have propagated outward (arrows), and the black-to-gray lines are the evolving displacement profiles over time. The vertical gray bars represent the location and age of onset for thermochronology sample transects (1–3), where the bar height indicates the age of onset. The dashed line in Figure 2b represents the various combinations of onset age that could result from fault segment linkage. The bottom row expresses the relative age relationships between each transect as predicted by each fault model.

The purpose of this paper is to describe a framework for using AHe to test conceptual models for fault growth. Substantial intracontinental extension in the Basin and Range Province has resulted in widespread exhumation of granitic plutons via normal faulting, making it a well-suited location for applying AHe thermochronology to investigate normal fault development. Thus, we apply our framework to a crustal-scale normal fault in the U.S. Basin and Range Province using data from multiple sample transects within the exhumed footwall of the fault. We then compare the framework to the conventional approach of using a single transect to illustrate its limitations. First, we review the current state of knowledge on fault growth by presenting the three main conceptual fault growth models (Figure 2): (a) tip propagation, (b) segment linkage, and (c) constant fault length. Next, we briefly introduce the fundamentals of low-temperature thermochronology and outline how the different faulting models would predict distinctive patterns in observed thermochronology data. Finally, we employ this approach by using two new and two existing cross sections with new ($n = 18$) and existing ($n = 16$) AHe sample data to investigate the evolution of the Jackson Mountains and Pine Forest Range in Nevada (Figures 4 and 5). Specifically, we sample a range of paleodepths in across-strike transects of the exhumed footwalls to quantify the spatiotemporal variability in exhumation due to fault slip and then evaluate our results against predictions implied by the different fault growth models. To our

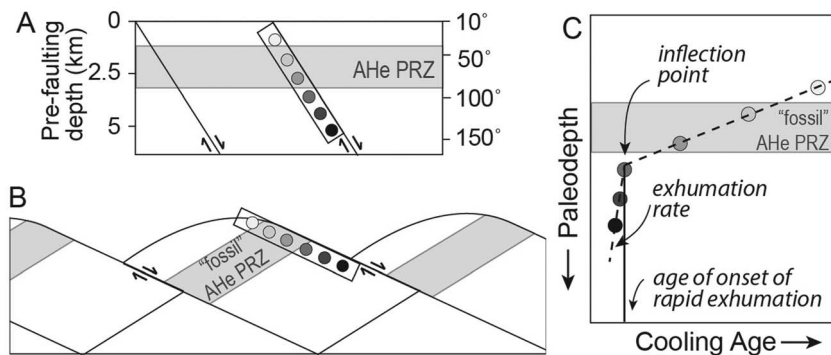


Figure 3. Schematic model of footwall exhumation (a) before and (b) after extension on normal faults with an apatite (U-Th)/He (AHe) sample transect (circles). Sample shading represents the gradational original paleodepths from most shallow (white) to deepest (black). Note how the preextensional AHe PRZ (Figure 3a) becomes exhumed by fault displacement (Figure 3b) creating a “fossil PRZ.” (c) Corresponding idealized AHe cooling age versus paleodepth plot. PRZ = partial retention zone (here ~40–85°C [after Farley, 2002]). Figure simplified from Stockli [2005] and Miller *et al.* [1999].

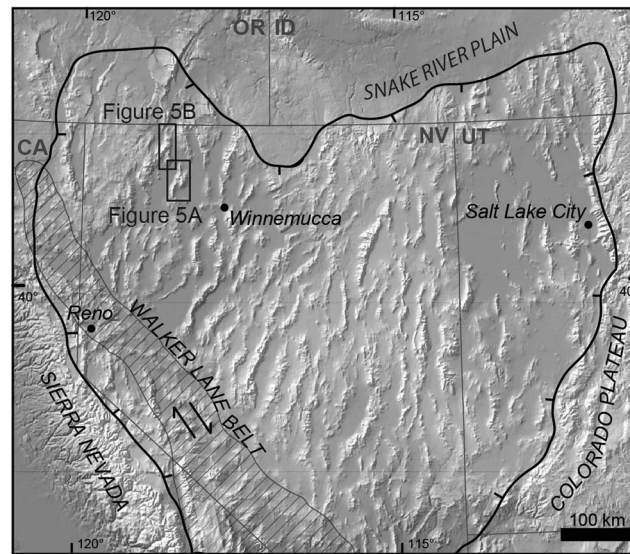


Figure 4. Map of the U.S. Basin and Range Province with related tectonic provinces and study area ranges highlighted in northwestern Nevada (compiled from *Faulds et al.* [2005] and *Colgan et al.* [2006a]). The thin gray lines are the state boundaries.

Schlische et al., 1996]). For example, faults that are tens of kilometers long have hundreds of meters of displacement, whereas faults a few meters in length have only a few centimeters of displacement. This scaling relationship appears to be a universal characteristic of unbounded (those not at plate boundaries) faults, holding true for faults with multiple segments, in all rock types, and all senses of slip [*Schlische et al.*, 1996, and references therein]. The conventional explanation for this observed D - L scaling is that it represents a growth relationship: faults grow by simultaneous increases in both length and maximum displacement. The fault dimensions change through tip propagation, which can be accompanied by linkage of previously isolated fault segments. However, it is also true that faults grow by the occurrence of repeated earthquakes superimposing slip on a fault plane. Observations of displacement and length of earthquake scarps suggest a linear relationship with a much lower D - L ratio than the cumulative displacement and length of mature fault systems ($D = 5 \times 10^{-5} L$; thick dashed line in Figure 1 [*Wells and Coppersmith*, 1994]). Reconciling D - L ratios from earthquake events to longer-term mature fault systems has led to an alternative fault growth model, whereby fault length is established early, with further growth dominated by displacement with little to no lengthening [*Walsh et al.*, 2002]. Thus, existing fault growth models can be divided into three main categories: lateral tip propagation, segment linkage, and constant fault length (Figure 2). In the next three sections, we describe the mechanical basis for each model and their predictions for the coevolution of fault length and displacement.

2.2. Tip Propagation Model

The tip propagation model is the conventional model for fault growth because it arises most directly from observed D - L scaling relationships (Figures 1 and 2a). Fault growth by lateral tip propagation relies on linear elastic fracture mechanics to explain the evolution of faults from inception to maturity [*Lin and Parmentier*, 1988; *Cowie and Scholz*, 1992a, 1992c]. Assuming an isolated fault, linear elastic fracture mechanics relates stresses at the tip of the fault to the energy required for the fault to propagate. When remote stress is applied to natural rock with infinite discontinuities (“Griffith cracks”), the stress concentrates at the tip of the crack. When the stress at the crack tip reaches a critical value (equal to the rock yield strength) the crack will propagate [*Lin and Parmentier*, 1988]. As a fault matures, deformation becomes more concentrated along a plane due to mechanical breakdown of rock decreasing the frictional resistance [*Cowie and Scholz*, 1992c]. Slip accumulates in the interior of the fault, increasing the stress concentrations at the fault tips and forcing the fault to grow laterally to ease those stress concentrations. This growth model predicts a scaling law between fault displacement and length and a displacement profile with a maximum in the fault center that tapers to zero at the tips, a relationship that has been documented by focused studies of fault dimensions [*Dugdale*, 1960; *Walsh and Watterson*, 1987; *Cowie and Scholz*, 1992a, 1992c]. In this model, a fault can be

knowledge, this is a novel application of AHe thermochronology to investigate normal fault propagation patterns that we hope inspires more use of isotope dating techniques to reconstruct how faults evolve in multiple directions.

2. Fault Growth and Thermochronology

2.1. Fault Growth Overview

Natural and theoretical fault systems appear to follow a relationship between the maximum displacement (D) and the length of a fault (L) that is described by the equation:

$$D = cL^n,$$

where c is a constant between $\sim 10^{-1}$ and 10^{-3} and n is between 1 and 1.5 (Figure 1 [*Walsh and Watterson*, 1988; *Cowie and Scholz*, 1992a, 1992c; *Gillespie et al.*, 1992; *Dawers et al.*, 1993;

A Jackson Mountains

B Pine Forest Range

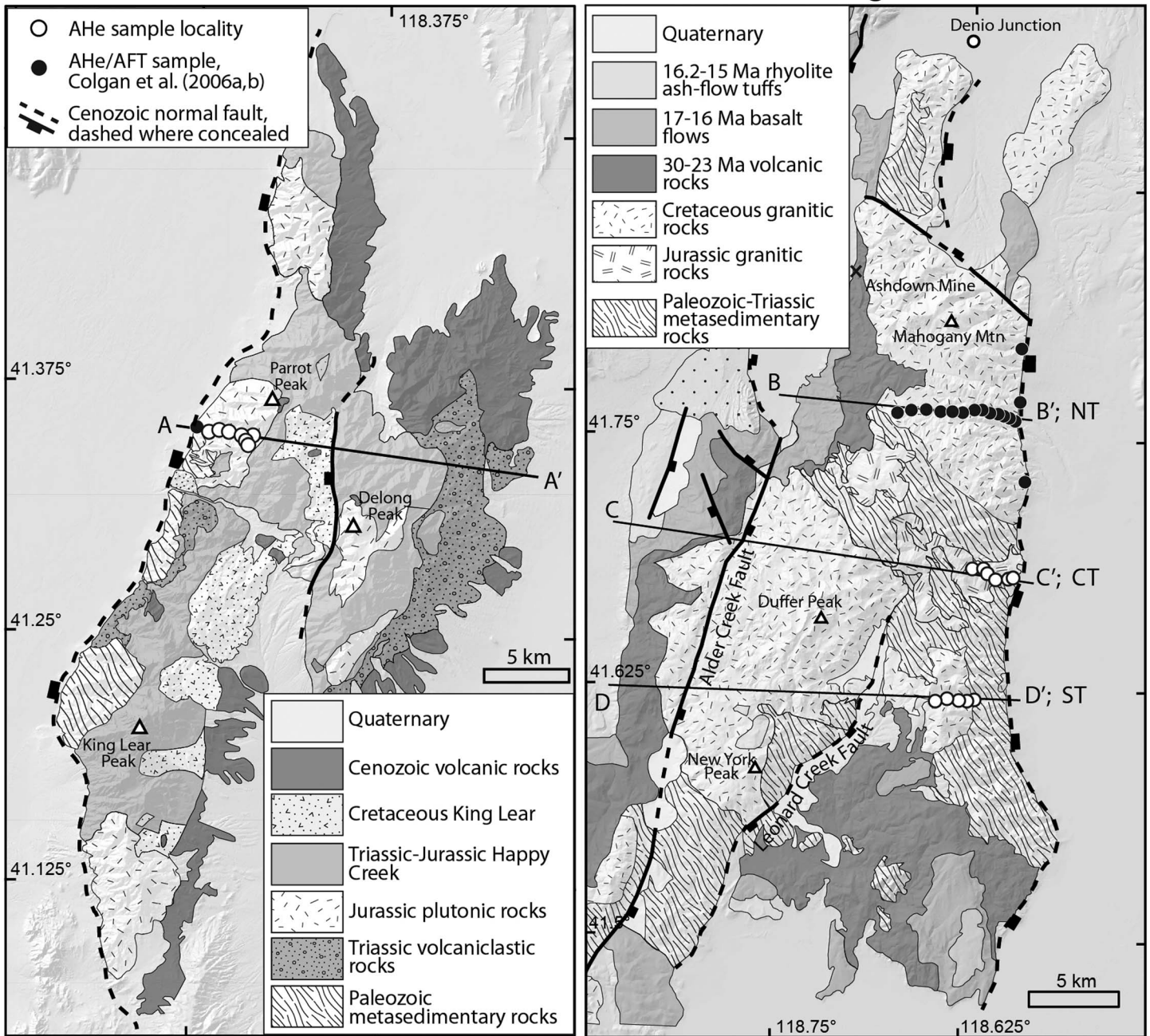


Figure 5. Generalized geologic maps and sample locations in the study area. (a) The Jackson Mountains from *Martin et al. [2010]*, *Quinn et al. [1997]*, and *Maher [1989]*. Cross section is in Figure 6. (b) The Pine Forest Range compiled from *Colgan et al. [2006b]*, *Wylid [1996]*, and *Smith [1973]*. NT = northern transect, CT = central transect, ST = southern transect. Cross sections are in Figure 7; horizon separation diagrams are in Figure 8.

envisioned as originating at a point and growing progressively by accumulating displacement and lengthening [*Scholz, 2002*].

Fault growth by segment linkage is a variant of the tip propagation model in which individual, adjacent segments grow by tip elongation until they ultimately behave as a single fault. Fault growth by segment linkage occurs when two or more isolated faults propagate toward each other and their stress fields begin to interact (Figure 2b). Faults usually occur in populations, and the interactions between faults may promote or inhibit fault growth, linkage, and coalescence [*Scholz, 2002*]. For example, when a fault ruptures it can

perturb the surrounding stress field, such that it increases the stress on a neighboring fault and thus the likelihood of a future earthquake [Cowie, 1998; Gupta and Scholz, 2000]. With continued interaction, the two en echelon tips will overlap, which decreases the shear stress and prohibits further propagation [Gupta and Scholz, 2000]. At this point, the two faults become mechanically linked, or “soft linked,” at the relay zone (overlap area between the en echelon segments), and as slip progresses some will come to behave as one fault (“hard linked”) equal to the combined length of the two segments, with displacement ultimately reaching a maximum at the collective fault center (e.g., displacement profiles in Figure 2b [Cartwright et al., 1995; Cowie, 1998; Gupta and Scholz, 2000]). Segment boundaries are often poorly defined but may be temporary locations of anomalously low displacement [Gupta and Scholz, 2000; McLeod et al., 2000]. Large, crustal-scale faults tend to form by slip on amalgamating segments, and the timing and magnitude of movement of each segment may vary (Figure 2b [Jackson and White, 1989; Scholz, 2002]).

2.3. Constant Fault-Length Model

In the constant fault-length model, fault length is established at an early stage of deformation, with additional fault slip accommodated by increases in displacement without significant further lengthening (Figure 2c). Field observations of historical earthquakes and mature fault systems show that both earthquake slip and finite displacement increase with fault length, but the respective scaling between the two is significantly different [Cowie and Scholz, 1992a; Wells and Coppersmith, 1994; Schlische et al., 1996]. When considering their dimensions, mature fault systems tend to have larger displacements for a given length than earthquake scarps (i.e., the D - L ratio is far smaller; Figure 1a). The constant fault-length model reconciles this discrepancy by requiring that a wide range of fault lengths be present at the early stages of deformation. The longest faults in the population will, initially, have displacements that are lower than conventional scaling predicts, but over time they will accumulate displacement with minor changes in length, ultimately reaching the observed D - L scaling relationship. Cessation of lengthening can occur if fault tips interact or encounter a barrier that retards propagation or if the fault inherits a predefined length from a preexisting structure [Walsh et al., 2002]. This model of fault growth is supported by a combination of natural observations, earthquake modeling, outcrops, and analog experiments [Morley, 1999; Childs et al., 2003; Schlagenhauf et al., 2008; Nicol et al., 2016].

2.4. Low-Temperature Thermochronology

Low-temperature thermochronology uses the temperature-dependent retention of radiogenic decay products to determine thermal histories of minerals at temperatures below $\sim 350^\circ\text{C}$ [Reiners et al., 2005]. The (U-Th)/He system exploits the alpha decay of ^{238}U , ^{235}U , ^{232}Th , and ^{147}Sm , which produces ^4He particles that are subsequently lost from apatite, zircon, and titanite grains by diffusion at elevated temperatures [Harrison and Zeitler, 2005]. The closure temperature (T_c ; the temperature above which ^4He is lost by diffusion [Dodson, 1973; Ketcham, 2005]) is different for each mineral system and is further affected by the cooling rate, size of the grains measured, radiation damage, and time-temperature (t - T) path; T_c increases with cooling rate, grain size, and amount of radiation damage [Farley, 2002; Reiners et al., 2005; Flowers et al., 2009]. Diffusion experiments on average-sized (<50 – $150\ \mu\text{m}$ diameter) apatite crystals show an average T_c of $68 \pm 5^\circ$, assuming a cooling rate of $10^\circ\text{C}/\text{km}$ [Farley, 2000]. At temperatures $>\sim 85^\circ\text{C}$, most ^4He is diffused out of the crystal as fast as it is produced; below $\sim 40^\circ\text{C}$ most ^4He is retained within the crystal. Between $\sim 85^\circ$ and $\sim 40^\circ\text{C}$, ^4He diffusion is variable; hence, this range is called the partial retention zone (PRZ) [Wolf et al., 1998; Farley, 2002]. Further complicating the system is slow ^4He loss at temperatures $<40^\circ\text{C}$ and minor ^4He retention at temperatures $>85^\circ\text{C}$ [Farley, 2000; Shuster et al., 2006]. Depending on the precise geothermal gradient, a reported AHe cooling age corresponds to passage through the upper 2–3 km of the crust, making it well suited to investigate recent thermal histories due to exhumation in the upper crust. For convenience, we often refer to a cooling age as indicative of a particular thermal event, but it is important to note that a measured AHe cooling age, as with any thermochronometric age, is the product of the complete t - T path of a sample.

The apatite fission track (AFT) method is sensitive to higher temperatures (~ 60 – 135°C ; equivalent to the upper 3–5 km of the crust) than the AHe system. Fission track dating exploits the fact that ^{238}U fission produces damage tracks in apatite crystals that progressively shorten (anneal) within the temperature interval ~ 110 – 60°C , termed the partial annealing zone (PAZ) [Green et al., 1989; Dumitru, 2000]. The rate at which fission tracks anneal and the temperature range over which they do is controlled by apatite composition,

orientation of tracks relative to crystallographic axes, and the thermal history (t - T) path of the sample [Green *et al.*, 1986; Ketchum, 2005]. Generally, shorter mean track lengths and a broader track-length distribution are characteristics of longer residence time within the PAZ and thus provide additional information on a sample's thermal history. A detailed explanation for applying AFT data to fault-driven exhumation can be found in Miller *et al.* [1999]. Below, we include existing AFT data [from Colgan *et al.*, 2006b] with new thermal history modeling to help quantify the onset of rapid exhumation.

2.5. Application to Normal Fault Systems

In extensional settings, footwall rocks are exhumed by fault motion in ways that can be quantified with thermochronologic data patterns and hence be used to test fault growth models (e.g., Figure 3). For example, prior to faulting a thermally equilibrated crustal block may have established an AHe PRZ (Figure 3a). Then, as faulting progresses, the block and the fossil PRZ are progressively exposed and cooled as a result of footwall uplift and/or exhumation (Figure 3b). To identify the onset of exhumation (and hence faulting), samples are collected along a transect parallel to transport direction (roughly perpendicular to fault strike) that spans the maximum exposed range of paleodepths [Spotila, 2005; Stockli, 2005]. Using this technique, samples are collected parallel to the extension direction (perpendicular to strike) and the cooling ages are evaluated as a function of paleodepth (Figure 3c). Ideally, paleodepth markers, such as stratified rocks that predate faulting, are present to provide a datum from which to calculate preextensional depth. Plotting cooling age versus paleodepth allows identification of an inflection point in the data trend that marks the base of the fossil PRZ and identifies the onset of rapid exhumation (Figure 3c [Fitzgerald and Gleadow, 1990; Stockli, 2005]). If fault slip has been of sufficient magnitude to exhume samples from below the preextensional PRZ (e.g., their thermochronometric clocks were completely reset prior to faulting), the cooling ages along the transect will document both when rapid exhumation initiated (the age at the inflection point) and the rate at which exhumation has occurred since then (the slope of the data; Figure 3c [Ehlers, 2005; Stockli, 2005]).

The three fault growth models described above predict distinctive thermochronologic age patterns provided that one key condition is met: enough slip has occurred to exhume some samples from high enough temperatures that (U-Th)/He and/or fission track "clocks" can record the faulting event (Figures 2 and 3). For example, if the tip propagation model best describes how a fault grows, then the fault center would begin rapid exhumation first, with progressively younger onset of rapid exhumation migrating outward as the fault lengthens and increases in displacement. Thus, a sample transect from the center of the footwall would possess the oldest onset of rapid exhumation, with progressively younger onset ages located toward the fault tips (Figure 2a). In practical terms, this means that the cooling age-elevation inflection point (Figure 3c) should decrease in age outward from the fault center along strike (Figure 2a). If the constant fault-length model is correct, the footwall would exhume as an intact block with little to no distinguishable difference in the onset age of rapid exhumation for any strike-perpendicular sample transects (Figure 2c). The segment linkage model does not have one predictable outcome but rather can fit in with the two mentioned above or be a different combination altogether (Figure 2b). For example, if the initial geometry involved two segments that eventually linked, the central region (representing the linkage point) may begin to rapidly exhume last (e.g., $1 \approx 3 > 2$; Figure 2b). We explore this and other possibilities in detail in section 6. To test these different models, we collected samples along a single, strike-perpendicular transect in the central Jackson Mountains (Figure 5a) and along three similarly oriented transects at ~8 km spacing along strike in the Pine Forest Range (Figure 5b).

3. Northwest Nevada: Geologic Setting

3.1. Geology

Much of the northern Basin and Range Province underwent a period of rapid extension beginning approximately 17–15 Ma (Figure 4 [Miller *et al.*, 1999; Snow and Wernicke, 2000; Stockli *et al.*, 2002; Colgan and Henry, 2009]). However, the northwestern Nevada portion remained comparatively undeformed until the late Miocene [Trexler *et al.*, 2000; Henry and Perkins, 2001]. Extension here began approximately 12–10 Ma and took place on widely spaced, high-angle normal faults that accommodated less extension than the closely spaced ("domino-style") fault systems and detachment faults found in the Basin and Range to the south and east [Colgan *et al.*, 2006a]. Footwall blocks of northwestern Nevada faults expose Paleozoic to

Mesozoic metasedimentary rocks intruded by Jurassic and Cretaceous granitic plutons [Wyld, 1996; Quinn *et al.*, 1997; Colgan *et al.*, 2006b; Martin *et al.*, 2010].

Basement rocks in the Jackson Mountains consist of Paleozoic to Mesozoic metasedimentary and volcanic rocks intruded by Jurassic plutons; all of which are unconformably overlain by Cretaceous sedimentary rocks (Figure 5a [Quinn *et al.*, 1997]). Most of the exposed rock is the Late Triassic to Early Jurassic Happy Creek Igneous Complex, a series of hypabyssal intrusive and volcanoclastic rocks [Quinn *et al.*, 1997]. These rocks were tilted and folded, then intruded by Jurassic (190–160 Ma) mafic to granitic plutons [Quinn *et al.*, 1997]. Sedimentary rocks of the Cretaceous King Lear Formation unconformably overlie all other units in the Jackson Mountains and are locally tilted 25–30° to the east (Figure 5a [Quinn *et al.*, 1997; Colgan *et al.*, 2006a]).

Basement rocks in the Pine Forest Range consist of Paleozoic to Triassic metavolcanic and metasedimentary rocks intruded by Cretaceous and Jurassic plutons (Figure 5b). All units were tilted, folded, and deformed under greenschist to amphibolite facies during Jurassic shortening. They were later intruded by Jurassic (200–185 Ma) and Cretaceous (116–98 Ma) granitic plutons that make up the majority of exposed basement in the study area [Smith, 1973; Wyld, 1996; Colgan *et al.*, 2006b].

Pre-Tertiary basement in the study area is unconformably overlain by volcanic rocks that blanketed the study area from the Eocene to the middle Miocene, filling in any previously developed topography on the basement surface and creating a low-relief volcanic plateau prior to extension [Brueseke *et al.*, 2008; Lerch *et al.*, 2008]. The Cenozoic volcanic section is broadly conformable and experienced no significant deformation from 35 to 16 Ma; prior to 35 Ma, the region was generally characterized by a tectonically stable land surface with only a few hundred meters of local topographic relief, up to ~800 m in paleovalleys [Faulds *et al.*, 2005; Colgan *et al.*, 2006b; Brueseke *et al.*, 2008; Lerch *et al.*, 2008]. We thus consider the paleodepth below the unconformity an appropriate proxy as a structural marker horizon [e.g., Colgan *et al.*, 2006a]. In the Pine Forest Range, volcanic rocks fall broadly into three groups by composition and age (Figure 5b). The oldest volcanic rocks range from 30 to 23 Ma and form an ~500 m thick sequence of older basalt flows, ash flow tuffs, tuffaceous sedimentary rocks, and hypabyssal intrusive rocks. Conformably overlying this sequence is a thick (up to 550 m) sequence of basalt flows with an $^{40}\text{Ar}/^{39}\text{Ar}$ whole-rock age of approximately 17–16 Ma [Colgan *et al.*, 2006b], correlated with the regionally extensive Steens Basalt [Camp *et al.*, 2013]. The Steens Basalt is overlain by a thin (<30 m) rhyolite ash flow tuff with an $^{40}\text{Ar}/^{39}\text{Ar}$ sanidine age of about 16.3 Ma [Colgan *et al.*, 2006b]. Cenozoic volcanic rocks are not widely exposed in the Jackson Mountains (Figure 5a), with the exception of basaltic-to-rhyolitic lava flows in the northern part of the range dated with $^{40}\text{Ar}/^{39}\text{Ar}$ sanidine to about 14.6 Ma [Castor and Henry, 2000]. Sections of volcanic and sedimentary rocks in both ranges are conformable and tilted up to 30° (Figures 6 and 7), indicating minimal tilting or faulting in the region prior to approximately 16 Ma [Colgan *et al.*, 2006b].

3.2. Cenozoic Normal Faulting

The Jackson Mountains are bounded to the west by a west dipping, dip-slip normal fault with a surface trace length of ~60 km (Figure 5a). The central Jackson Mountains are cut by the DeLong Peak fault, a minor west dipping fault striking ~20 km down the center of the range [Quinn *et al.*, 1997]. There is no direct evidence for the dip of these faults, but they are assumed to be ~40° by analogy to the nearby Pine Forest Range and Santa Rosa Range faults [Colgan *et al.*, 2006a]. Assuming 1–2 km of sedimentary basin fill [after Saltus and Jachens, 1995], >1 km of Cretaceous sedimentary section, and 2–4 km of Triassic–Jurassic igneous rocks, it is estimated that ~7–8 km of total slip has occurred along the two faults (Figures 5a and 6 [Maher, 1989; Quinn *et al.*, 1997; Colgan *et al.*, 2006a; Martin *et al.*, 2010]).

The Pine Forest Range is bounded to the east by an east dipping, dip-slip normal fault with a surface trace length of ~40 km (Figure 5b). Where exposed, the fault plane dips 40°E and has well-developed striations indicating dip-slip movement [Colgan *et al.*, 2006b]. In the northern half of the range, the footwall is uniformly tilted as an intact block. In the southern part of the range, the footwall is cut by two additional normal faults with minor slip, the Alder Creek and Leonard Creek faults. Gravity data suggest ≤1 km sedimentary fill in the adjacent valley [Saltus and Jachens, 1995]; including 0.5–1.1 km of Cenozoic volcanic section and 1–3 km of exhumed Mesozoic igneous and metamorphic rock, it is estimated that 7–9 km of total slip and ~3–3.5 km of vertical throw accumulated on the range-front fault (Figures 5b and 7 [Smith, 1973; Wyld, 1996; Colgan *et al.*, 2006b]).

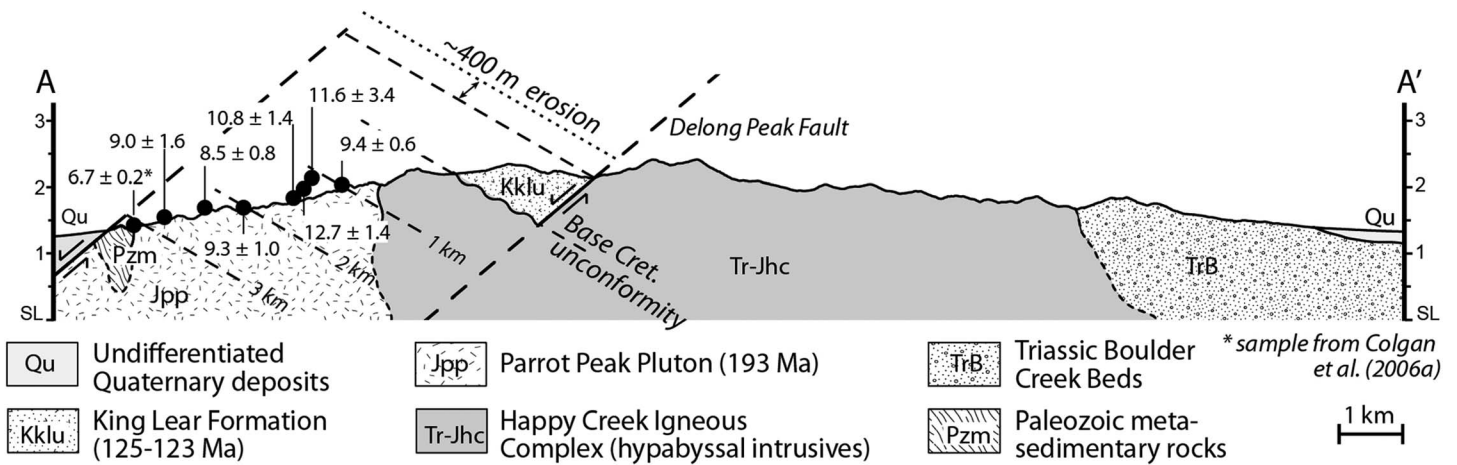


Figure 6. Jackson Mountain geologic cross section showing structural positions of samples (black circles) with their (U-Th)/He cooling ages in Ma (Table 1). The cross section is modified from Colgan *et al.* [2006a]. We used the basal Cretaceous unconformity as a structural datum, and show the interpreted missing Cretaceous section (see text for explanation). See Figure 5a for the location. SL = sea level. The vertical and horizontal scales are the same.

Many normal faults in the Basin and Range are arrays that may have initiated as segments before coalescing into coherent structures [e.g., Cowie *et al.*, 2000]. The fault traces in the study area are moderately sinuous (Figure 5), which may reflect the locations of previously isolated segments. Growth of the Jackson Mountains and Pine Forest range-front faults may have involved amalgamation of distinct segments, but their modern continuous traces suggest that they are now behaving as cohesive structures. For simplicity,

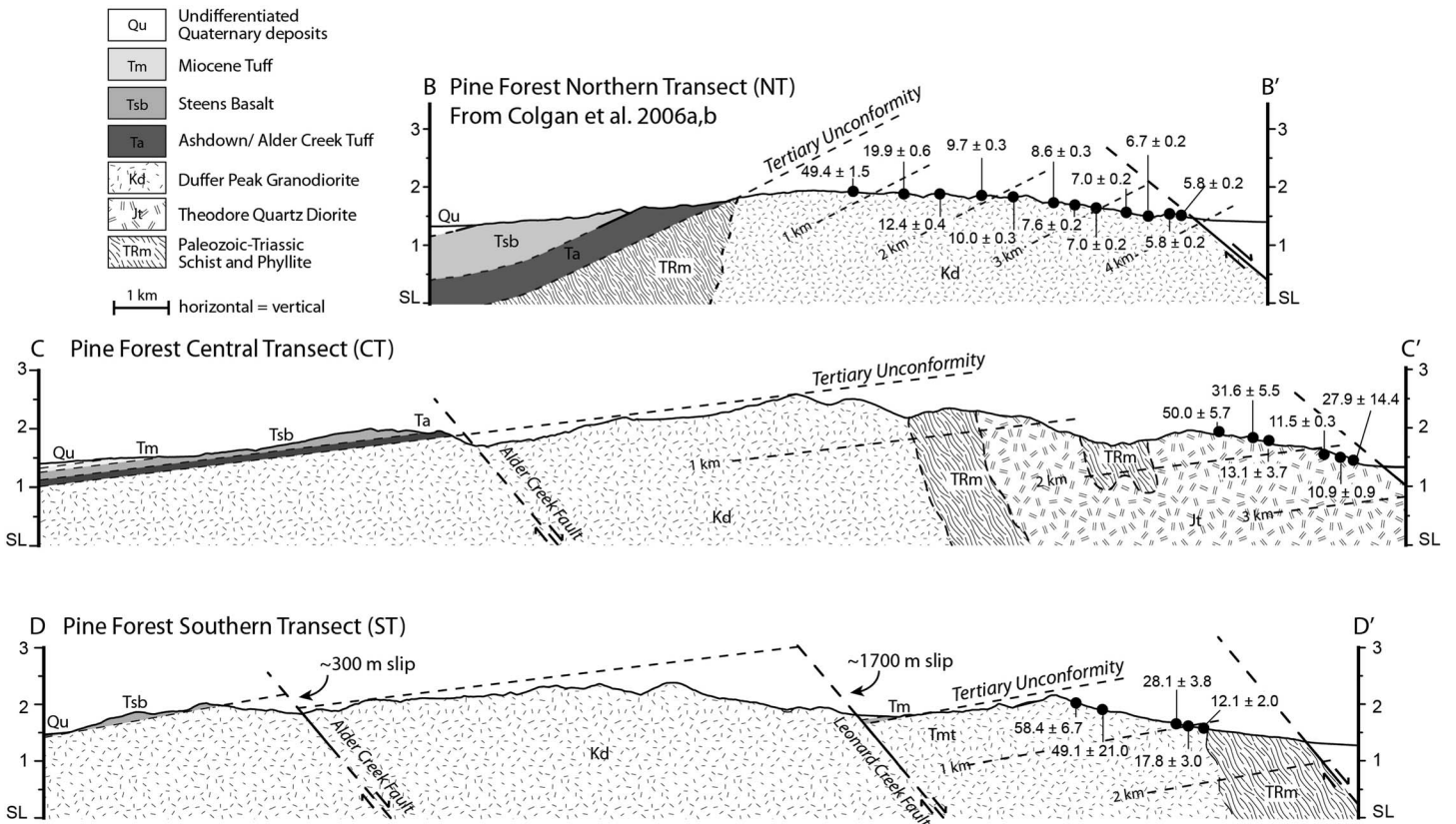


Figure 7. Geologic cross sections through the Pine Forest Range showing structural position of samples (black circles) analyzed with their (U-Th)/He cooling ages in Ma (see also Table 1). SL = sea level. The northern transect (NT; B-B') is modified from Colgan *et al.* [2006a]. The central transect (CT; C-C') and southern transect (ST; D-D') are new in this study. See Figure 5b for the locations. SL = sea level. The vertical and horizontal scales are the same.

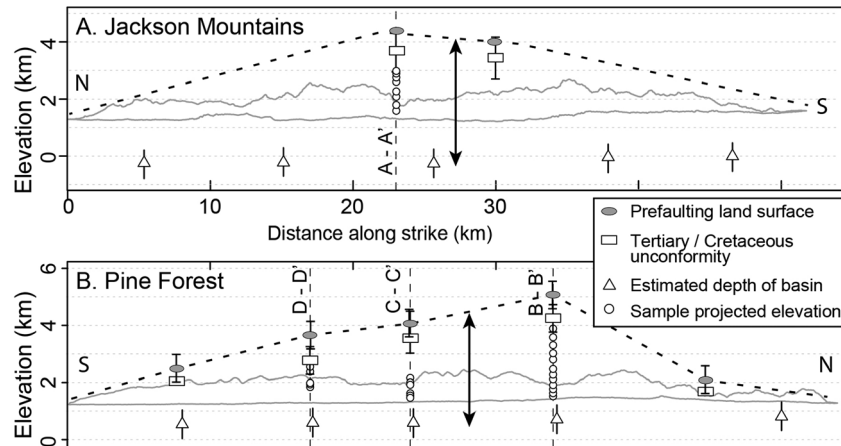


Figure 8. (a and b) Horizon-separation profiles showing elevation of range crests and fault traces (gray lines). Samples (white circles), unconformities (white rectangles), and pre-faulting land surface (gray ovals) projected onto a vertical plane parallel to the fault trace. The dashed line is the estimated throw based on projection of pre-faulting land surface. For the Jackson Mountains throw is a minimum estimate and is based on projection of Cretaceous unconformity plus 1400 m of eroded material (see text). Basin depth (triangles) estimated from gravity map of *Saltus and Jachens* [1995]. The vertical arrows indicate the approximate fault throw.

we thus view these faults as behaving like single traces characterized by a displacement maximum near their along-strike centers for much of their history. We also revisit this issue later on in the discussion.

4. Methods

We completed mineral separations using standard crushing, gravimetric, and magnetic techniques at the University of North Carolina at Chapel Hill. We selected single apatite crystals based on size (>60 μm in diameter), morphology (free of major scratches and preference to double termination), and lack of inclusions. We analyzed them for U, Th, Sm, and He at the University of Colorado at Boulder in the Colorado Thermochronology Research and Instrumentation Laboratory. We then performed inverse thermal history modeling of the AHe cooling age results with HeFTy version 1.9.1 [Ketcham, 2005, 2016] using the most modern calibration model for apatite: the radiation damage accumulation and annealing model (RDAAM) [Flowers *et al.*, 2009] with the age alpha correction of Ketcham *et al.* [2011]. The use of RDAAM as a calibration model is best practice for modeling AHe data, as each new model builds on and improves past models (R. Ketcham, personal communication 2016). Our exhumation calculations assume a T_c of 65°C (for 50 μm half-width grains and a cooling rate 15–25°C/Myr [e.g., Farley, 2000]), a surface temperature of 10°C, and a stable geothermal gradient of 27°C/km [after Colgan *et al.*, 2006a]. The assumed geothermal gradient is based on paleodepths of the exhumed AFT PAZ and AHe PRZ and is consistent with Miocene geothermal gradients estimated in other studies [Fitzgerald *et al.*, 1991; Foster *et al.*, 1991; Stockli, 1999; Stockli *et al.*, 2002; Colgan *et al.*, 2006a]. A detailed explanation of the data and methods used to calculate the geothermal gradient can be found in Colgan *et al.* [2006a]. We note that the modern geothermal gradient in the study area is much higher (~54°C/km [Blackwell and Richards, 2004; Coolbaugh *et al.*, 2005]), but the late Miocene geothermal gradient is more relevant to our data, since it presumably prevailed during the onset of slip on the faults in question. Detailed analytical methods and thermal history modeling parameters and diagrams are in the supporting information.

We also report geologic cross sections for each sample transect (Figures 6 and 7a modified from Colgan *et al.* [2006a, 2006b]) and horizon-separation profiles (Figure 8) based on existing maps and structural measurements [Smith, 1973; Maher, 1989; Wyld, 1996; Quinn *et al.*, 1997; Colgan *et al.*, 2006b; Martin *et al.*, 2010]. To calculate the preextensional depths of apatite samples, we projected the basal Tertiary unconformity (Cretaceous unconformity in the Jackson Mountains) across the range at angles consistent with field measurements. For the Pine Forest Range, we then added the thickness of the Miocene volcanic section (~900–1000 m) to the reconstructed vertical depth of each sample below the unconformity. We use D_s to denote sample depth beneath the pre-faulting land surface [after Colgan *et al.*, 2006a]. This preextensional

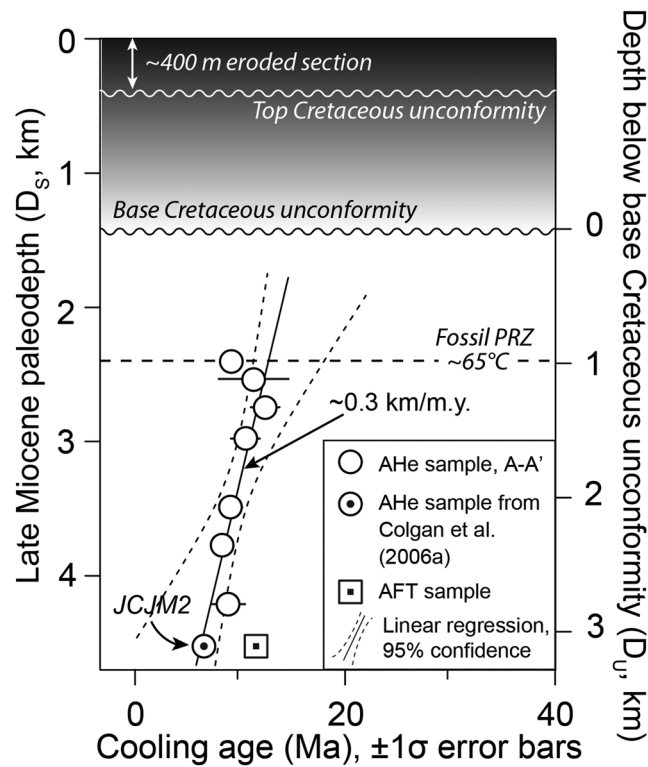


Figure 9. Jackson Mountain AHe and AFT cooling age versus paleodepth plot for a sample transect (A-A'; locations in Figure 5a). AHe = apatite (U-Th)/He; AFT = apatite fission track; PRZ = partial retention zone; D_s = preextensional paleodepth. The fossil PRZ is calculated based on $T_c = 65^\circ\text{C}$ and a geothermal gradient of $27^\circ\text{C}/\text{km}$. Ages are means of one to five individual grains (see Tables 1 and S1 and Figure S1 for full analytical results).

S1 in the supporting information [e.g., Brichau et al., 2006; Flowers et al., 2008]), with the exception of MEJM23, for which we have only a single-grain cooling age (Table 1). We note that four samples (MEJM22, MEPF07, MEPF25, and MEPF24) have particularly poor reproducibility within the sample (i.e., widespread in the individual crystal ages and characterized by a standard deviation >6 Ma). We report the mean ages of these four samples for completeness but avoid emphasizing these mean ages in our discussion (see Table 1). We also briefly summarize relevant existing AHe and apatite fission track (AFT) data from the Pine Forest Range northern transect (NT; Tables 1 and 2 [Colgan et al., 2006a, 2006b]). Full new analytical results are in the supporting information.

5.1. Overview

We analyzed 18 new samples from granitic to dioritic plutons with 1–5 single-grain AHe ages per sample (Tables 1 and S1). These samples were collected to complement 16 existing samples from previous studies (Figure 5 (black circles) and Tables 1 and 2 [Colgan et al., 2006a, 2006b]). AHe ages in the study area range from approximately 58.4 to 3.3 Ma and are from samples exposed over >700 m in mean topographic relief from the fault-proximal flanks of the Pine Forest and Jackson Mountain ranges (Figures 5–8). Age uncertainties of the new data for single-grain ages include error associated with alpha ejection corrections and are $\sim 10\%$ of the age (Tables 1 and S2); age uncertainties of the data previously reported [i.e., from Colgan et al., 2006a] do not include error associated with alpha ejection correction and are $\sim 2\%$ of the age. Reported age uncertainty on the mean age is 1 standard deviation of the mean (Table 1). Measured effective uranium (eU) concentrations on individual grains range from 3.1 to 173 ppm (majority between 20 and 40 ppm; Table S1 and Figure S2 in the supporting information) and show no systematic correlation with cooling age (Figure S2). We collected some of these samples ($n=7$) from a strike-perpendicular transect in the Jackson

depth (D_s) includes the Cenozoic volcanic cover (Cretaceous section for the Jackson Mountains) and is used for interpreting the timing and rate of exhumation as a proxy for fault slip (e.g., Figure 3c).

5. Results

We present AHe analyses along three new across-strike sample transects and one previously reported across-strike sample transect [Colgan et al., 2006a] from the footwalls of the Pine Forest Range and the Jackson Mountains (Figures 5–11). For each transect, we present the sample cooling ages, their total paleodepth (D_s), their depth below the Tertiary (Pine Forest Range) or Cretaceous (Jackson Mountains) unconformity, and associated exhumation magnitudes and rates. The value reported for total paleodepth (D_s) is equivalent to exhumation magnitude; we use the “total paleodepth” terminology to remain consistent with previous work [Colgan et al., 2006a, 2006b]. For each sample we note intrasample variability of eU (effective uranium; equivalent to $U + 0.235$ Th), grain size, and He content. The mean age is reported for all samples (two to five crystals; Table

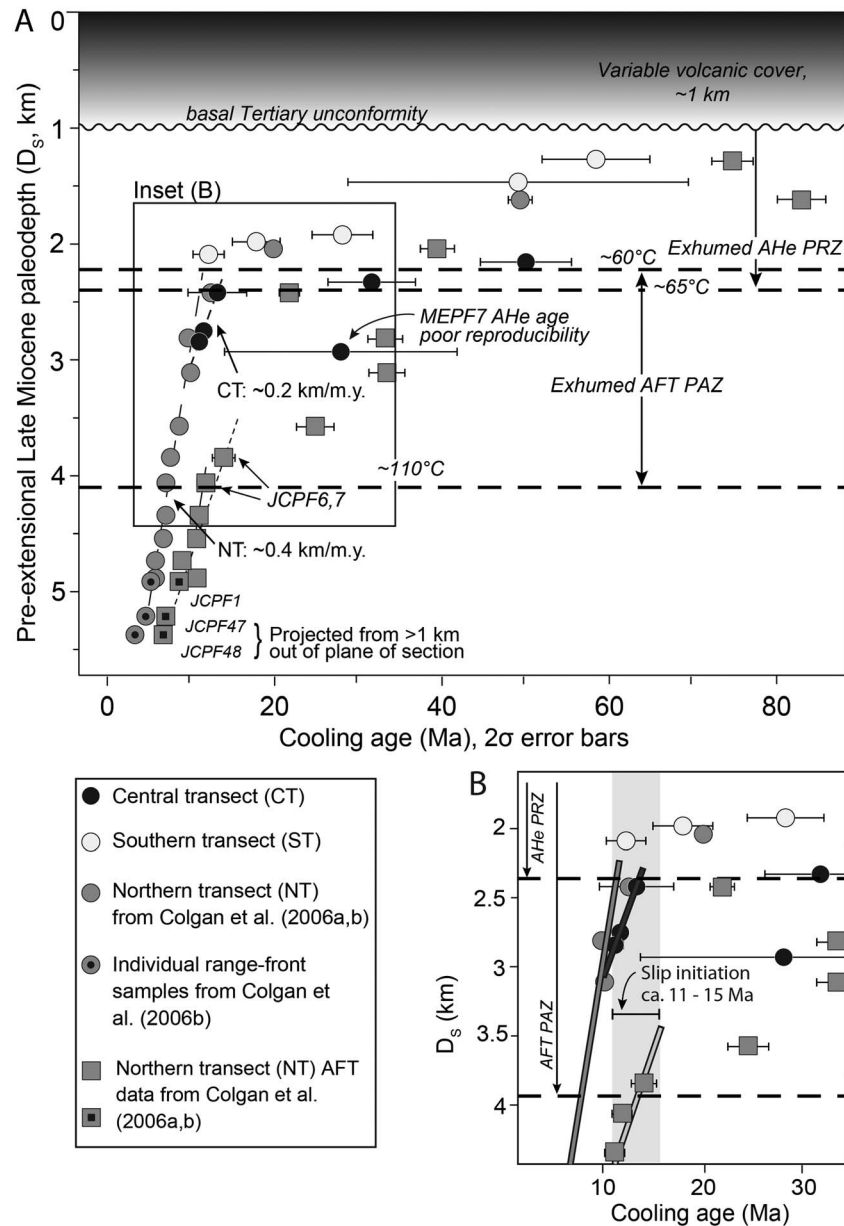


Figure 10. Pine Forest Range thermochronology data. AHe = apatite (U-Th)/He; AFT = apatite fission track; PRZ = partial retention zone; PAZ = partial annealing zone; D_s = preextensional paleodepth. The horizontal dashed lines are the estimated paleodepths of AHe and AFT-related paleo T_c values (see section 4 for the explanation). (a) Cooling age versus paleodepth plot for the three sample transects (locations in Figure 5b). AHe ages are means of two to five individual grains (see Tables 1 and S1 and Figure S1 for full analytical results). AFT cooling ages are shown for the northern transect (data from Colgan et al. [2006a, 2006b]). (b) Inset of the preextensional AHe PRZ, AFT PAZ, and inflection points in age-elevation relationships that estimate the onset of rapid exhumation (proxy for fault initiation). The gray bar highlights the range of possible initiation ages within data uncertainty.

Mountains (Figures 5a and 6) to supplement an existing range-front sample [Colgan et al., 2006a]. We also collected new samples ($n = 11$) along two strike-perpendicular transects in the Pine Forest Range (CT and ST; Figures 5b and 7) to complement another existing strike-perpendicular transect (NT, $n = 13$ samples; Figure 7) and three additional single, range-front samples [Colgan et al., 2006a, 2006b]. Our new samples came from unaltered, unweathered Mesozoic granite to granodiorite, which yielded good-quality apatite crystals. Sample MEJM22 came from unaltered, unweathered Mesozoic diorite that also yielded good-quality crystals.

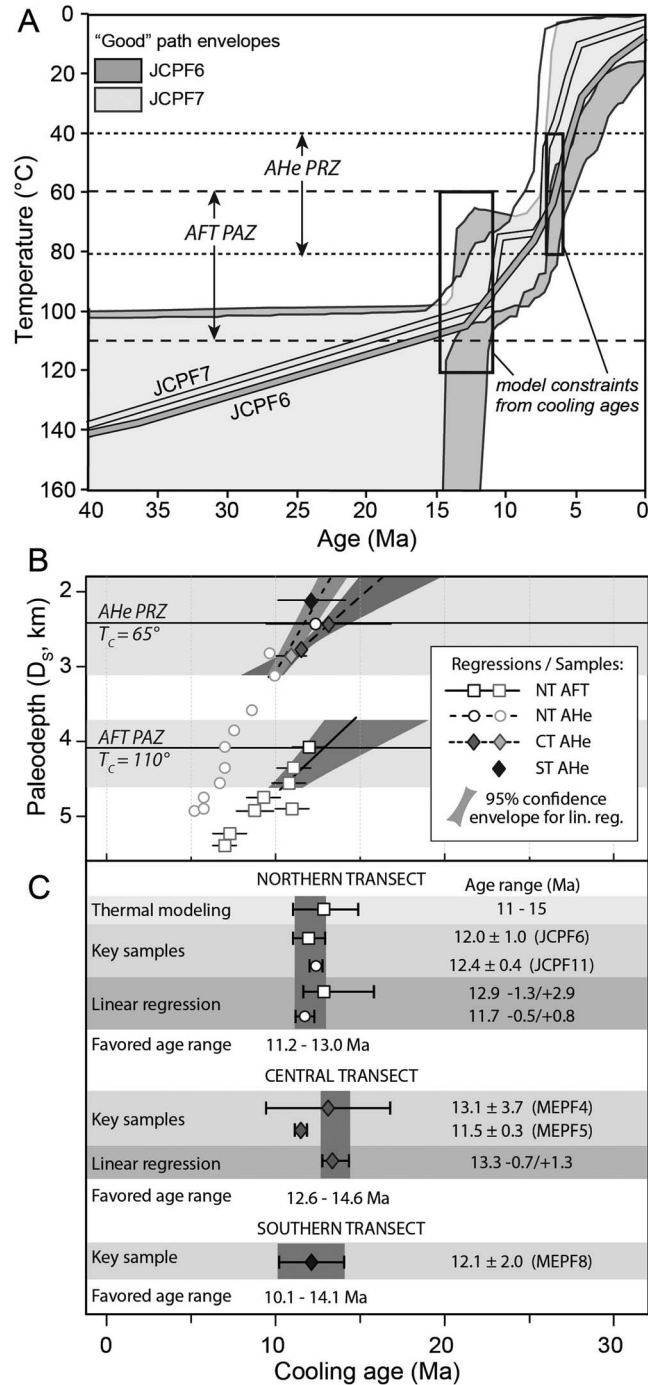


Figure 11. Identifying the onset of Pine Forest rapid exhumation with multiple approaches. (a) Thermal modeling for two key AFT samples in the northern transect (NT). Samples JCPF7 and JCPF6 bound the onset of rapid cooling with their AFT cooling age (Figure 10). Inverse modeling envelopes that encompass all the “good fit” simulations (gray areas) and weighted mean paths (thick gray lines) to the data for both samples. The not shown initial boundary conditions are crystallization ages at 100–120 Ma. (b) Age versus paleodepth for samples at or below the fossil PRZ/PAZ and linear regression model fits with 95% confidence envelopes. The gray bars around the T_c depth are the range of depths possible if the geotherm and T_c are varied from 24 to 27°C/km and 55 to 75°C, respectively. (c) Exhumation onset estimates from (1) thermal modeling, (2) cooling age and uncertainty of key samples, and (3) the intersection of linear regressions (with 95% confidence envelopes) of all samples from below the PRZ/PAZ with the depth of T_c .

Table 1. Apatite (U-Th)/He Data and Estimated Sample Paleodepths

Sample	X (UTM ^a)	Y (UTM ^a)	D_S (m) ^b	D_U (m) ^b	He Age (Ma \pm 1 σ) ^c					n^d	Pooled He Age (Ma \pm 1 σ) ^e
					Apatite 1	Apatite 2	Apatite 3	Apatite 4	Apatite 5		
Jackson Mountains (A-A'); JCM2 from <i>Colgan et al.</i> [2006a]											
JCM2	373310	4580106	4517	3100	6.7 \pm 0.4	6.6 \pm 0.4				2	6.7 \pm 0.2
MEJM20	373474	4578799	4207	2790	7.0 \pm 0.6	8.4 \pm 0.6	10.5 \pm 1.5	10.7 \pm 0.8	8.3 \pm 0.6	5	9.0 \pm 1.6
MEJM19	374066	4578948	3769	2352	7.8 \pm 0.6	7.9 \pm 0.6	8.6 \pm 1.3	9.7 \pm 0.9	8.6 \pm 1.0	5	8.5 \pm 0.8
MEJM18	374627	4578705	3486	2069	10.8 \pm 1.2	8.9 \pm 1.1	8.6 \pm 0.6	9.8 \pm 0.9	8.3 \pm 0.6	5	9.3 \pm 1.0
MEJM17	375388	4578558	2978	1561	12.8 \pm 0.9	10.5 \pm 0.8	11.3 \pm 0.8	9.0 \pm 0.6	10.5 \pm 0.8	5	10.8 \pm 1.4
MEJM23	375505	4578270	2745	1328	12.7 \pm 1.4					1	12.7 \pm 1.4
MEJM22	375517	4577986	2535	1118	14.0 \pm 1.0	9.2 \pm 0.8				2	11.6 \pm 3.4
MEJM16	376073	4578628	2400	983	9.1 \pm 0.9	9.3 \pm 0.7	8.8 \pm 0.6	10.3 \pm 1.4	9.5 \pm 0.7	5	9.4 \pm 0.6
Pine Forest northern transect (B-B'); ages from <i>Colgan et al.</i> [2006b]											
JCPF2	367432	4624359	4880	3780	5.2 \pm 0.3	6.3 \pm 0.3				2	5.8 \pm 0.2
JCPF3	367135	4624549	4730	3630	5.2 \pm 0.3	6.3 \pm 0.3				2	5.8 \pm 0.2
JCPF4	366860	4624647	4540	3440	6.6 \pm 0.4	6.8 \pm 0.4				2	6.7 \pm 0.2
JCPF5	366514	4624715	4340	3240	7.6 \pm 0.5	6.4 \pm 0.4				2	7.0 \pm 0.2
JCPF6	366054	4624786	4060	2960	6.6 \pm 0.4	7.4 \pm 0.4				2	7.0 \pm 0.2
JCPF7	365665	4624978	3840	2740	7.4 \pm 0.4	7.7 \pm 0.5				2	7.6 \pm 0.2
JCPF8	365226	4624986	3570	2470	8.3 \pm 0.5	8.9 \pm 0.5				2	8.6 \pm 0.3
JCPF9	364553	4624814	3110	2010	9.9 \pm 0.6	10.4 \pm 0.6				2	10.0 \pm 0.3
JCPF10	363977	4624886	2810	1710	10.1 \pm 0.6	9.2 \pm 0.6				2	9.7 \pm 0.3
JCPF11	363307	4624899	2420	1320	12.2 \pm 0.7	12.6 \pm 0.8				2	12.4 \pm 0.4
JCPF12	362523	4624976	2040	940	19.9 \pm 1.2	19.8 \pm 1.2				2	19.9 \pm 0.6
JCPF13	361737	4624929	1620	520	51.8 \pm 3.1	46.9 \pm 2.8				2	49.4 \pm 1.5
Pine Forest range-front samples; ages from <i>Colgan et al.</i> [2006b]											
JCPF1	367775	4625401	4910	3810	4.8 \pm 0.3	5.6 \pm 0.3				2	5.2 \pm 0.15
JCPF47	367807	4628393	5210	4110	3.8 \pm 0.4	5.4 \pm 0.3				2	4.6 \pm 0.2
JCPF48	368039	4620985	5370	4270	3.6 \pm 0.2	3.0 \pm 0.2				2	3.3 \pm 0.1
Pine Forest central transect (C-C')											
MEPF2	365087	4616161	2154	1554	52.6 \pm 6.0	42.9 \pm 4.7	55.3 \pm 5.6	54.4 \pm 7.3	44.9 \pm 6.5	5	50.0 \pm 5.7
MEPF3	365702	4616146	2328	1728	33.4 \pm 2.6	31.9 \pm 2.5	37.1 \pm 2.7	24.0 \pm 3.0		4	31.6 \pm 5.5
MEPF4	365933	4615884	2418	1818	10.4 \pm 0.8	16.6 \pm 2.0	8.6 \pm 0.6	13.1 \pm 1.1	17.0 \pm 2.5	5	13.1 \pm 3.7
MEPF5	366371	4615561	2751	2151	11.5 \pm 1.0	11.3 \pm 1.2	11.4 \pm 1.1	12.0 \pm 0.9		4	11.5 \pm 0.3
MEPF6	367072	4615582	2843	2243	12.4 \pm 1.7	11.2 \pm 1.4	10.2 \pm 1.5	10.4 \pm 1.8	10.8 \pm 1.9	5	10.9 \pm 0.9
MEPF7	367333	4615653	2930	2330	26.1 \pm 2.0	36.3 \pm 4.2	14.3 \pm 1.0	15.0 \pm 2.1	47.9 \pm 5.1	5	27.9 \pm 14.4
Pine Forest southern transect (D-D')											
MEPF8	365192	4608870	2088	1088	13.7 \pm 1.2	23.8 \pm 1.8 ^f	12.4 \pm 1.8	13.0 \pm 2.2	9.2 \pm 1.6	4	12.1 \pm 2.0
MEPF27	364931	4608868	1980	980	15.7 \pm 1.1	19.8 \pm 1.8	33.7 \pm 4.0 ^f			2	17.8 \pm 3.0
MEPF26	364719	4608836	1921	921	26.0 \pm 4.5	32.6 \pm 3.4	29.7 \pm 3.2	24.2 \pm 1.9		4	28.1 \pm 3.8
MEPF25	363410	4609077	1466	466	48.9 \pm 6.2	28.2 \pm 2.0	70.3 \pm 8.3			3	49.1 \pm 21.0
MEPF24	362936	4608903	1269	269	65.8 \pm 4.7	49.8 \pm 3.8	57.2 \pm 4.6	60.7 \pm 6.7		4	58.4 \pm 6.7

^aUTM zone 11°N.

^b D_S denotes the sample depth relative to the pre-faulting land surface, including Tertiary volcanic (Pine Forest Range) or sedimentary overburden (Jackson Mountains). For Jackson Mountains, these values were calculated based on assumed geothermal gradient and T_c , thus having \pm 300 m of uncertainty. D_U is the depth measured from the structural datum (Tertiary or Cretaceous unconformity).

^cSingle-grain uncertainty is the analytic uncertainty plus the uncertainty related to the alpha ejection correction, which is calculated using the method of *Farley* [2002].

^d n is the number of grains for average age calculation.

^eReported ages are averaged for number of reproducible crystals (n) in each sample. Results characterized by anomalously old ages, attributed to parentless He or unidentified inclusions, are excluded from calculation of mean. Uncertainty here is \pm 1 standard deviation of the mean.

^fIndividual crystal ages excluded from mean calculation due to anomalous ages and poor reproducibility.

5.2. Jackson Mountains

5.2.1. Single Transect (A-A')

AHe ages from the central Jackson Mountains transect range from approximately 14.0 to 6.7 Ma and overall young toward the range-bounding fault trace (Figure 6). Because Cenozoic rocks are not exposed along the entire range (Figure 5a), we estimated paleodepths using the basal Cretaceous unconformity as a preextensional horizontal surface (Figure 6 [after *Colgan et al.*, 2006a]). The depths below the base-Cretaceous

Table 2. Apatite Fission Track Data from Colgan *et al.* [2006a, 2006b]

Sample	AFT Age (Ma $\pm 1\sigma$)	Track Length ($\mu\text{m} \pm 1\sigma$)	D_s (m) ^a
Jackson Mountains (A-A')			
JCM2	11.7 \pm 1.5	14.15 \pm 0.15	4517
Pine Forest northern transect (B-B')			
JCPF2	11.0 \pm 1.0	13.31 \pm 0.28	4880
JCPF3	9.3 \pm 1.0	13.83 \pm 0.37	4730
JCPF4	10.8 \pm 1.0	14.05 \pm 0.51	4540
JCPF5	11.1 \pm 1.0	14.03 \pm 0.21	4340
JCPF6	12.0 \pm 1.0	13.76 \pm 0.38	4060
JCPF7	14.0 \pm 1.2	13.08 \pm 0.22	3840
JCPF8	24.7 \pm 1.9	12.10 \pm 0.31	3570
JCPF9	33.7 \pm 1.8	12.57 \pm 0.14	3110
JCPF10	33.1 \pm 1.7	12.67 \pm 0.11	2810
JCPF11	21.8 \pm 1.1	14.67 \pm 0.12	2420
JCPF12	39.2 \pm 1.9	13.43 \pm 0.10	2040
JCPF13	83.1 \pm 2.8	13.61 \pm 0.09	1620
Pine Forest range-front samples			
JCPF1	8.8 \pm 1.1	13.85 \pm 0.45	4910
JCPF47	7.3 \pm 1.0	ND ^b	5210
JCPF48	7.0 \pm 0.7	14.06 \pm 0.14	5370

^a D_s denotes the sample depth relative to the pre-faulting land surface, including Tertiary volcanic and sedimentary overburden.

^bND denotes no data.

unconformity range from 983 to 3100 m (D_u); unfortunately, no sample appears to have been exhumed from within or above the preextensional AHe PRZ (e.g., the kink in Figure 3c) as evident from the age-paleodepth relationship, and thus, all ages record ongoing rapid cooling in the Cenozoic (Figure 9). Although the data do not constrain the onset of rapid exhumation, they do permit a new estimate for the thickness of Cretaceous section (~1.4 km, with 0.4 km eroded) because they all indicate exhumation from below T_c . Using a geothermal gradient of 27°C/km and T_c of 65°C, the paleodepths (D_s) of the samples span 2400–4517 m (± 300 m; Table 1 and Figures 6 and 9). The youngest cooling age is 6.7 \pm 0.2 Ma (JCM2) from 3100 m depth below the basal Cretaceous unconformity (4517 m total paleodepth; Table 1), indicating that at least 2 km of exhumation occurred since that time in order to bring that sample

to the surface. The oldest single-grain cooling ages are 12.7 \pm 0.9 and 14.0 \pm 1.0 Ma (MEJM23 and MEJM22, respectively), indicating that rapid exhumation was ongoing by approximately 13 Ma, which is consistent with the available AFT data from Colgan *et al.* [2006b, Table 2]. Regression of the age-paleodepth data for the eight samples below the fossil PRZ suggests onset of exhumation at 12.6 + 5.3/–1.5 Ma (95% confidence; asymmetry is due to uncertainty envelope on the regression) at an exhumation rate of ~0.3 km/Myr (Figure 9). Applying that exhumation rate to the ~2 km of post-6.7 Ma exhumation indicated by sample JCM2 suggests that faulting has continued until the present. In summary, the data indicate ongoing rapid exhumation from approximately 13 to present at ~0.3 km/Myr that has ultimately exhumed ~4.5 km so far (maximum D_s = 4517 m).

5.3. Pine Forest Range

5.3.1. Central Transect (CT; C-C')

Six AHe ages from the central Pine Forest Range transect range from approximately 50.0 to 10.9 Ma and young toward the range-bounding fault (C-C'; Figures 5b and 7). The samples span 1554–2330 m depth below the Tertiary unconformity or 2154–2930 m total paleodepth (D_s) assuming ~600 m of volcanic cover (Figure 7). A fossil PRZ is evident in the age-paleodepth plot, where sample MEPF4 (age = 13.1 \pm 3.7 Ma) marks the inflection between different age-paleodepth relationships (black circles in Figure 10 and Table 1). However, there are insufficient samples from within or above the fossil PRZ to quantify the early Miocene and older cooling history. Below the fossil PRZ, at $D_s \geq 2.4$ km, cooling ages decrease from 13 to 10.9 Ma. Linear regression of these data shows rapid footwall exhumation at a rate of ~0.2 km/Myr beginning at 13.3 + 1.3/–0.7 Ma (95% confidence; Figure 10). This scenario is further supported by thermal history modeling (Figure S2). The youngest recorded cooling age is 10.9 \pm 0.9 Ma (MEPF6) from D_s = 2843 m. At least ~2.1 km of post-11 Ma exhumation is indicated by this sample and ~3 km of total exhumation assuming a 27°C/km geothermal gradient.

The sample with the greatest paleodepth (MEPF7; D_s = 2930 m) has wide scatter in the ages of the five analyzed individual grains and anomalously high ages given the expectation for this sample to have the youngest cooling ages in the transect (ages range from 14.3 \pm 1.0 Ma to 47.9 \pm 5.1 Ma; Table 1). Unfortunately, there is no obvious explanation for the age scatter within these data. Intrasample variability is not uncommon in (U-Th)/He ages and can be due to a number of potential causes including differences in grain size, U- and/or Th-rich inclusions, or zoning that were not identified during sample preparation,

significant parentless He, or it may be that this part of the pluton had unrecognized nearby intrusions or hot springs [e.g., Fitzgerald *et al.*, 2006].

5.3.2. Southern Transect (ST; D-D')

Five AHe ages from the southern Pine Forest Range transect range from approximately >60 to 12 Ma and young toward the range-bounding fault (D-D'; Figures 5b and 7). This transect is 7 km south along strike from the central transect (Figure 5b), and samples span 269–1088 m depth below the Tertiary unconformity or 1269–2088 m in total paleodepth, assuming ~1 km of volcanic cover (Figure 7 and Table 1). In this part of the range, the sampled pluton does not reach the range-bounding fault (Figure 5b), thus limiting the exposed paleodepths accessible for analysis due to paucity of apatite in exposed metamorphic rock adjacent to the fault (Figure 5b). As a result, all the samples appear to be from within or close to the base of the exhumed PRZ and no break in slope is evident in the age-paleodepth relationship (light gray circles in Figure 10). Furthermore, the individual cooling ages within the samples (excluding MEPF8) have poor reproducibility, possibly due to extended time within the PRZ. The youngest cooling age is 12.1 ± 2.0 Ma from sample MEPF8, 1088 m below the Tertiary unconformity (2088 m total paleodepth). The deep paleodepth and cooling age reproducibility for this sample suggest that it was at or near the base of the preexhumation PRZ and is thus a good bracket for the timing of exhumation. This transect shows >2.1 km of exhumation since approximately 12 Ma (minimum 2.1 km from total paleodepth [D_s] of MEPF8; 2.7 km is the estimated paleodepth of the range front based on the cross section; see Figure 7c), suggesting an exhumation rate of 0.2 km/Myr. Due to the lack of samples from deeper paleodepths, we cannot be certain that this youngest sample indicates the onset of rapid exhumation due to fault slip. However, the data suggest that at 12.1 ± 2.0 Ma the sample was at $T_c = 65^\circ\text{C}$ or greater and has since been exhumed ~2–3 km at a minimum exhumation rate of 0.2 km/Myr. This scenario is strongly supported by thermal history modeling results (Figure S3).

5.3.3. Northern Transect (NT; B-B') from Colgan *et al.* [2006a, 2006b]

The northern Pine Forest Range transect includes 12 AHe ages ranging from approximately 49.4 to 5.8 Ma that also young toward the range-bounding fault (B-B'; Figures 5b and 7 [Colgan *et al.*, 2006a]). The samples span 520–3780 m depth below the Tertiary unconformity and 1620–4880 m in total paleodepth (D_s ; Figure 7). The base of a fossil PRZ is evident in the age-paleodepth relationship at $D_s = \sim 2.3$ km (Figure 10). Samples JCPF11–13 have cooling ages of ~50–13 Ma and come from total paleodepths of <2400 m, indicating that they were exhumed prior to reburial beneath ~1 km of volcanic rocks between 30 and 16 Ma (see Colgan *et al.* [2006a] for further discussion). Below the lower boundary of the fossil PRZ at $D_s > \sim 2.3$ km, cooling ages decrease from approximately 10.0 to 5.8 Ma. Linear regression of these data shows rapid cooling via footwall exhumation beginning at $11.7 + 1.3/-0.7$ Ma at a rate of ~0.4 km/Myr (~2.1 km over ~5 Myr). Thermal history modeling of the data supports this scenario (Figures 11a and S3). The youngest cooling age is 5.8 ± 0.2 Ma from sample JCPF2, $D_s = 4880$ m, indicating ~2 km of post-6 Ma and 4.5–5 km of total exhumation assuming a geotherm of $27^\circ\text{C}/\text{km}$ [after Colgan *et al.*, 2006a].

AFT ages measured by Colgan *et al.* [2006a, 2006b] for this transect range from approximately 83.1 to 9.3 Ma and also young toward the range-bounding fault (Table 2 [Colgan *et al.*, 2006a, 2006b]). Samples JCPF6 and JCPF7 are particularly important because they bracket the inflection point on the AFT age-depth curve and thus define the onset of rapid cooling (Figure 10). Sample JCPF7 is from $D_s = 3840$ m and has AFT cooling age of 14.0 ± 1.2 Ma, with shorter track lengths (mean = $13.1 \mu\text{m}$; Table 2). Sample JCPF6 is from $D_s = 4060$ m and has AFT cooling age of 12.0 ± 1.0 Ma, with long track lengths (mean = $13.8 \mu\text{m}$; Table 2). Sample JCPF7 is interpreted to be the deepest sample from within the fossil PAZ, and JCPF6 the shallowest, fully reset sample from below the fossil PAZ.

5.3.4. Isolated Range-Front Samples

Three isolated samples collected from the range front of the central to northern Pine Forest Range have the youngest AHe ages, ranging from approximately 5.2 to 3.3 Ma (Figures 5b and 10 and Table 1 [Colgan *et al.*, 2006a, 2006b]). These samples span the deepest sampled total preextensional paleodepths (D_s) of 4910–5370 m. The youngest sample, JCPF48, is located ~3 km south of the northern transect (Figure 5b). It records a cooling age of 3.3 ± 0.1 Ma from $D_s = 5370$ m, indicating ~2 km of post-3 Ma exhumation assuming a geotherm of $27^\circ\text{C}/\text{km}$ [after Colgan *et al.*, 2006a]. These very young AHe cooling ages document the most recent exhumation, providing evidence for continued slip on the range-bounding fault.

6. Discussion

6.1. Limitations of a Single Sample Transect

As we did in the Jackson Mountains, it is common to analyze thermochronometer samples along a single, sample elevation profile to quantify normal fault-driven exhumation [e.g., *Stockli et al., 2003; Colgan et al., 2006a; Fosdick and Colgan, 2008*]. Although our data failed to capture the position of the fossil PRZ (Figure 9), two key observations emerge from the data set. First, all samples have middle to late Miocene cooling ages that record ongoing, rapid exhumation due to normal faulting and suggest that their preextensional paleodepths were sufficiently deep to be below AHe T_c . Assuming that $T_c = 65^\circ\text{C}$ (based on grain size and cooling rate [e.g., *Farley, 2000*]) and the geotherm is $27^\circ\text{C}/\text{km}$ [after *Colgan et al., 2006a*], the paleodepth of T_c here is ~ 2400 m, requiring ≥ 400 m of section eroded in the middle to late Mesozoic from the Cretaceous King Lear Formation in order for the shallowest paleodepth sample to be at or below T_c (Figures 6 and 8). Second, the data show that exhumation was ongoing since approximately 13 Ma and that faulting may have continued to the present at a rate of ~ 0.3 km/Myr, ultimately exhuming ~ 4.5 km. This age of onset and exhumation rate are consistent with regional mid-Miocene normal faulting in the northwestern Basin and Range Province [*Colgan et al., 2006a, 2006b*]. In general, if a sample transect spans a wide range of paleodepths and contains samples that span both within and below the fossil PRZ (e.g., those that exclusively record fault-driven exhumation), this two-dimensional approach can tell us (1) when rapid exhumation began and (2) the rate and duration of the exhumation. Because the primary mechanism for exhumation in this setting is normal faulting, we can assume that the exhumational signal here is equivalent to the tectonic signal, thus recording fault slip [e.g., *Ring et al., 1999*]. Therefore, while these data are useful for addressing basic tectonic questions about the regional onset, rate, and magnitude of faulting, they cannot address models for fault growth that predict characteristic tip elongation behavior—this requires data that span a substantial amount of the fault length in the along-strike direction. We focus the remainder of our discussion on the Pine Forest Range, where three separate transects inform our interpretation of both the across- and along-strike dimensions of fault growth.

6.2. Timing of Fault Growth

Given the data resolution, the Pine Forest Range thermochronology results show that faulting began in all sampled areas between approximately 15 and 11 Ma (gray box in Figure 10b). Determining fault initiation from a cooling age–elevation data set is inherently uncertain because (a) locating the inflection point age is limited by the data uncertainties and (b) closure temperatures in apatite grains can vary due to variations in helium diffusion kinetics [*Farley, 2000; Flowers et al., 2009; Shuster and Farley, 2009*]. AHe age analytical precision for our data is $\sim 2\%$ and expands to $\sim 6\text{--}10\%$ when the alpha ejection estimate is applied [*Ehlers and Farley, 2003*]. Thus, within the resolution of our data, our results indicate that faulting began concomitantly in all sampled regions. This principal result provides no clear evidence to support the tip propagation model of fault growth and hence suggests that the segment linkage or constant fault-length models may be more applicable to the Pine Forest Range.

For robust interpretation of the thermochronometer data to evaluate fault growth, we combine three approaches to limit the range of resolvable thermal histories given cooling age uncertainties: (1) inverse thermal history modeling, (2) sample cooling ages, and (3) linear regression modeling (Figure 11). First, we performed inverse thermal history modeling with HeFTy software [*Ketcham, 2016*] of the two samples that bracket the AFT inflection point (JCPF6 and JCPF7; Tables 1 and 2 and Figures 10a and 11a) in the northern transect. We use both the AHe and AFT cooling ages as model constraints (black boxes in Figure 11a). These results show that rapid cooling initiated between approximately 15 and 11 Ma, identified by the inflection point in the sample paths (Figure 11a). Second, we compile the cooling ages that have the shallowest paleodepths but are still located beneath the fossil PAZ/PRZ (in other words, the first samples exhumed from below T_c ; Figures 11b and 11c). These cooling ages are the first to indicate cooling from a completely reset state and provide a minimum age by which rapid exhumation began. Because the first sample from below the fossil PAZ/PRZ is based on an interpreted location of the PAZ/PRZ, which in itself is subject to uncertainty, we developed a third estimate by computing linear regressions and 95% confidence envelopes for all samples from below the fossil PRZ/PAZ (Figure 11b). In this case, the range of possible onset ages is the confidence envelope of the regression at the location of the estimated PAZ/PRZ (dark gray envelopes in Figure 11b). Because the Pine Forest southern transect lacks samples from below the fossil PRZ, it is excluded from this

particular analysis. We acknowledge the caveat that applying a linear regression model to the reset samples assumes that the exhumation rate was steady, which may not be the case. However, it provides a range of plausible, quantitative dates for the onset of rapid exhumation.

Figure 10 reveals two major insights: one, confidence in interpretations of ages of onset is ultimately only as good as the data resolution itself. Two, the more thermochronometers used, the more constraints available for the thermal history interpretation and thus the onset of rapid exhumation. It is important to employ several methods for estimating the rapid cooling onset age because low-temperature thermochronometer systems are sensitive to variations in grain properties, the environment, cooling rates, and the t - T path of the sample [Farley, 2000; Ketcham, 2005; Shuster *et al.*, 2006; Flowers *et al.*, 2009]. For example, depending on the precise T_c , two AHe samples in the Pine Forest southern transect are potentially the first exhumed from below T_c (MEPF4 with a mean age of 13.3 ± 3.7 Ma and MEPF5 with a mean age of 11.5 ± 0.3 Ma). Picking only one of these AHe samples to indicate the onset of fault-driven exhumation could result in an error of ~ 5 Myr. MEPF5 has better reproducibility and lower uncertainty in the pooled age, providing strong evidence that faulting was ongoing by approximately 11.5 Ma. In this case, linear regression may be a more appropriate estimation of the onset of faulting, which puts the range at $13.3 + 1.3/-0.7$ Ma (Figure 11c). However, linear regressions are only as good as the data they are based upon and are skewed by outliers. For example, in the AFT data from the Pine Forest Range northern transect, the linear regression envelope is affected by a single sample with a somewhat anomalous age (JCPF2 with an AFT age of 11.0 ± 1.0 Ma). Combining several methods allows for a more thorough interpretation of the data. Using multiple thermochronometers can also better constrain the onset of rapid exhumation [e.g., Balestrieri *et al.*, 2003; Colgan *et al.*, 2008]. Because they are sensitive to different temperatures, employing both AFT and AHe systems tightly brackets the window within which faulting began. Examination of the five estimates for the northern transect (white symbols in Figure 11c) shows that the overlap for rapid cooling onset is between 12.0 and 12.5 Ma; this age range falls within error of every method employed, resulting in the most narrow possible window for fault initiation. Collectively, the data show that rapid cooling commenced in all transects sometime between 15 and 11 Ma (gray box in Figure 11b).

Our Pine Forest Range results are consistent with the constant fault-length model for fault growth. The Pine Forest Range footwall began to exhume at all sample locations between 15 and 11 Ma, possibly bringing the range-front fault to near its modern length no later than ~ 10 –8 Ma or no more than 3–4 Myr after faulting began. These results are consistent with studies that show that faults reach their final length within 1–3 Myr or at least document slowed lateral propagation compared to displacement within that time frame [Meyer *et al.*, 2002; Morewood and Roberts, 2002; Walsh *et al.*, 2002; Gawthorpe *et al.*, 2003; Amos *et al.*, 2010]. In these cases, fault length appears to increase rapidly and then tip propagation slows or ceases over $> \sim 10^6$ year time scales. In some instances, initial rapid fault lengthening can be attributed to reactivation and exploitation of preexisting fault planes [Walsh *et al.*, 2002]. In others, the cessation of fault lengthening can occur due to interaction with another fault and/or some other type of geologic barrier that retards propagation [Nicol *et al.*, 1996; Manighetti *et al.*, 2001; Mouslopoulou *et al.*, 2009]. Furthermore, as faults penetrate deeper crustal depths they encounter increased confining pressure and different mechanical properties, resulting in conditions favorable to higher D - L ratios [Gudmundsson, 2004]. Displacements and lengths of crustal-scale faults cutting the entire seismogenic crust may also be limited mechanically by the depth to the brittle-ductile transition [Scholz and Contreras, 1998; Watts and Burov, 2003]. We speculate that these are all likely possibilities in the Basin and Range Province because the region possesses numerous interacting extensional faults; the largest of which cut the entire seismogenic crust and might also overprint preexisting contractional or volcanic structures that remain buried beneath the Cenozoic basin deposits [e.g., King *et al.*, 1988; Wernicke, 1992].

6.3. Exploring Fault-Length Growth Scenarios

The onset of rapid exhumation due to faulting is equivalent at all three sample transects within the resolution of the thermochronology data, which provides a 4 Myr window of 15–11 Ma. Our interpretation is that the data are best explained with the constant fault-length model of growth. Here we explore alternative fault evolution scenarios that still fit our data. In each case, the end result is that the fault reached its modern fault length within 3–4 Myr of onset (10–8 Ma), providing further support for the constant fault-length model of growth.

Let us assume that linear regression of the age-paleodepth relationships from the Pine Forest Range accurately indicates fault onset age at each transect (i.e., where the linear model intersects the fossil PRZ; Figure 11b). In this thought experiment, our results show a difference in timing of 1.6 Myr in onset of slip

along the range-front fault (Figure 11b). In detail, faulting began in the central Pine Forest Range at ~ 13.3 Ma, then at ~ 11.7 Ma in the northern Pine Forest Range 9 km farther north along strike (Figure 8b). We further speculate that the youngest recorded cooling age (~ 12.1 Ma) in the southern portion brackets the onset of rapid exhumation as supported by thermal history modeling (Figure S3). These best fit results generate a unidirectional lateral fault propagation rate of ~ 6 km/Myr. In other words, if slip initiated near the fault center, it propagated both north and south at 6 km/Myr or lengthened 12 km/Myr total. The additional young, isolated AHe ages along the range front show that exhumation continued beyond ~ 5 – 3 Ma (samples JCPF1, JCPF47, and JCPF48 in Table 1). Because the modern Pine Forest Range fault trace is $\sim <50$ km long, this collective exhumation pattern suggests that the fault would have reached its current length within ~ 3 – 4 Myr of onset (by ~ 10 – 8 Ma). In this situation, all further slip occurred by displacement accumulation with negligible lengthening. Thus, even in this idealized case, our results suggest that displacement accumulation can occur with little to no simultaneous lengthening.

Basin and Range extensional faults range from tens of meters to tens of kilometers in length. Many of the kilometer-scale faults are arrays that may have initiated as isolated segments that have coalesced into cohesive arrays [e.g., Cowie *et al.*, 2000]. Here we explore this possibility for the Pine Forest range-front fault using an approach that combines fault *D-L* scaling and thermochronology data to envision how both data sets might be brought together to quantify fault growth (Figure 12). We assume that (1) each sample transect represents a fault segment but acknowledge that many segmentation possibilities exist; (2) each segment length scales linearly with displacement (for which exhumation magnitude is used as a proxy) by a factor of 0.1 to 0.03 as predicted by *D-L* scaling data (Figure 1) [Cowie and Scholz, 1992b, 1992c; Dawers *et al.*, 1993; Schlische *et al.*, 1996; Densmore *et al.*, 2004]; and (3) because of point 2, the fault segments initially obey the tip propagation model for fault growth. The thermochronologic data are consistent with the idea that the central fault segment began slipping first, then the southern segment, both with an exhumation rate of ~ 2 km/Myr (Figures 10, 12a, and 12b). The northern segment began slipping last but at a faster rate of ~ 4 km/Myr (Figures 10 and 12b). Maximum fault segment length estimates (calculated using $c = 0.03$; Figure 1a [Densmore *et al.*, 2004]) suggest that they were already overlapping by 10 Ma (Figure 12c). In contrast, the lower segment length estimates (calculated using $c = 0.1$) suggest that they were overlapping by 8.5 Ma and the total fault length was ~ 30 km, which approaches the modern length (Figure 12d). We conclude that, if the fault was originally segmented, individual segments could have been interacting and hence likely hard linked prior to ~ 8.5 Ma. This thought experiment (a) emphasizes that *D-L* scaling and cooling age data can complement each other and (b) shows that the range-front fault has been at or near its modern fault length for a majority ($>65\%$) of its existence, providing further support for the constant fault-length model.

Our data also suggest that fault-driven exhumation is reduced in the central and southern Pine Forest Range compared to the northern region (Figures 7 and 10). Results from the northern transect show rapid exhumation starting at $11.7 \pm 0.8 / -0.5$ Ma at a rate of ~ 0.4 km/Myr, ultimately exhuming almost 5 km to the surface (Figures 7 and 10) [Colgan *et al.*, 2006a]. In contrast, the central transect began rapid cooling at approximately $13.3 \pm 1.3 / -0.7$ Ma at a rate of ~ 0.2 km/Myr, ultimately exhuming ~ 3 km; exhumation in the southern transect is bracketed by the youngest AHe cooling age, 12.1 ± 2.0 Ma, indicating a minimum exhumation rate of ~ 0.1 km/Myr, ultimately exhuming ~ 1.5 km. The northern part of the range is an intact footwall block that is tilted with no major faults aside from the range-front fault (Figure 5b). To the south, the footwall is broken by the Alder Creek and Leonard Creek normal faults that have varying degrees of offset (Figures 5b and 7). We infer that the greater degree of exhumation in the north is because all extension has been taken up on a single fault rather than partitioned across several faults as it is in the central and southern portions of the range. An alternate explanation is that the evolution of this fault may have involved an overall trend of displacement increasing in magnitude and rate from south to north. However, we emphasize that this variation in exhumation rate and magnitude does not affect our primary interpretation that the fault reached its modern fault length within ~ 3 – 4 Myr of initiation.

6.4. Implications for Fault Growth

Our observations appear to contradict the conventional tip propagation fault growth model in which displacement accumulation and lengthening are simultaneous (Figure 2a). This model is based primarily on *D-L* data sets that span 7 orders of magnitude [Schlische *et al.*, 1996, and references therein]. If faults do not grow

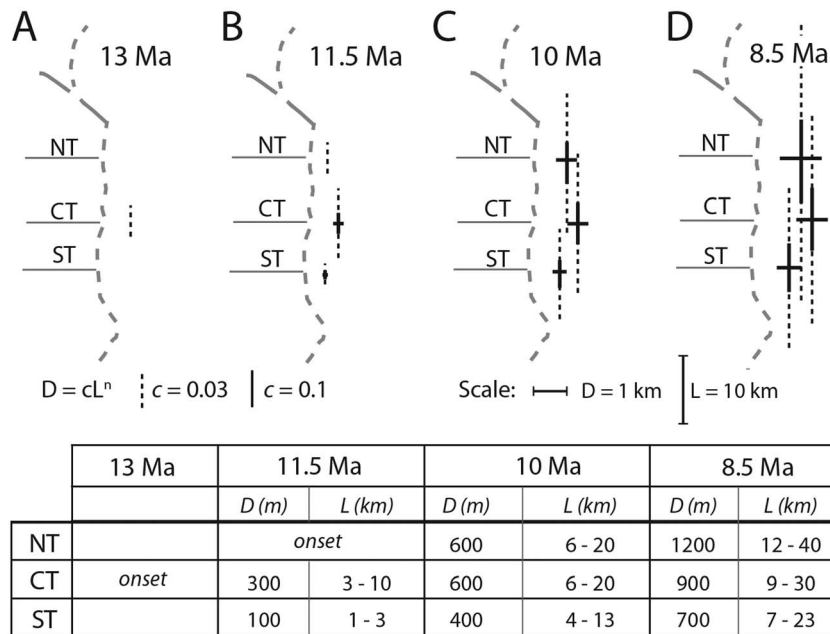


Figure 12. Spatiotemporal growth estimates for Pine Forest Range faulting estimated with fault scaling and thermochronology data. (a–d) Fault growth from inception at 13 Ma until 8.5 Ma shown in 1.5 Myr increments. Fault segment length is calculated using the displacement (*D*)-length (*L*) scaling relationship $D = cL^n$ with $c = 0.1$ (shorter, solid line), $c = 0.03$ (longer, dashed line), and $n = 1$ (after Figure 1) with the values listed in the table. We substituted exhumation magnitude from the thermochronology data (Figures 7 and 9) as a proxy for *D*. The gray dashed lines are the modern surface trace of the Pine Forest range-front fault (after Figure 5b). NT = northern transect, CT = central transect, ST = southern transect; 5:1 exaggeration on the displacement:length ratio.

in this manner, what explains the observed scaling relationship? Many researchers have pointed out that combining data sets to interpret fault scaling is problematic [Scholz and Cowie, 1990; Cowie and Scholz, 1992a; Wojtal, 1994; Clark and Cox, 1996; Kim and Sanderson, 2005] and that there is poor correlation between *D* and *L* within individual data sets [Schlische et al., 1996, and references therein]. These issues stem in part from the difficulty in measuring *D* and *L* consistently across length scales using different methods that each possesses unique biases. Interpretations of the scaling relationship are further complicated by observations that the *D*-*L* ratio of faults increases through time (higher displacement for a given length) [Morewood and Roberts, 1999; Morley, 1999; Walsh et al., 2002; Childs et al., 2003; Amos et al., 2010]. Thus, it has been proposed that for some fault systems, (a) the observed scaling relationship in Figure 1a more properly represents mature fault geometry rather than the actual growth process and (b) that depending on the earthquake recurrence interval, fault dimensions could reach the mature scaling ratio in $\leq 30\%$ of its life span (between 2 kyr and 2 Myr [Walsh et al., 2002]). Our interpretation of Pine Forest fault growth does not contradict the observed global fault *D*-*L* scaling relations but rather suggests that the constant fault-length model more accurately describes how fault growth was achieved.

This study has two main implications for the growth of the Pine Forest Range fault and possibly other crustal-scale extensional faults. First, our data show that range-front fault slip has not involved steady and continuous radial propagation (e.g., Figure 1b). For simplicity, fault growth tends to be modeled in a 2-D plane of observation (i.e., the Earth’s surface) and the propagation direction is assumed to be in plane [e.g., Cowie et al., 2000]. In these models, fault propagation is radial, occurring continuously toward the tip lines that results in a displacement profile with a central maximum and propagation only observable on the 2-D observation plane (Figure 1b). Considering 3-D fault growth requires acknowledgement that (1) the 2-D plane of observation may not be a perfect cross section through the fault and (2) propagation likely occurs out of the plane of observation [Walsh et al., 2003; Kim and Sanderson, 2005]. Recognition of these limitations imposed by the observation plane serves to explain how the Pine Forest Range could continue to accumulate displacement without observable fault trace lengthening. Second, the range-front fault trace length may have been established by ~ 10 –8 Ma despite possible influence of fault segmentation affecting

displacement accumulation. Theoretical models supported by field observations indicate that kinematically interrelated fault segmentation is a common feature of faults across scales [Cowie, 1998; Walsh *et al.*, 2003; Soliva *et al.*, 2008]. Positions of the Pine Forest range-front fault and nearby Leonard Creek and Adler Creek faults suggest that some interaction is responsible for the higher exhumation magnitude in the north, as slip was increasingly partitioned across three subparallel faults toward the south (Figure 5b). The degree to which the range-front fault was segmented early on is beyond the scope of this study, but if it was initially segmented, the individual segments probably amalgamated to its near modern geometry prior to ~8 Ma (Figure 12).

6.5. Implications for Fault-Driven Topographic Growth

Several studies have exploited idealized fault growth models to represent the tectonic boundary condition in order to assess the response of topography to fault slip at the range scale [e.g., Densmore *et al.*, 2004, 2007b; Barnes *et al.*, 2011; Whittaker, 2012]. For example, if faults grow in a continuous and radial manner according to the conventional fault growth model (Figure 2a), then a space-for-time substitution can be applied to examine the topographic response to fault slip [Harbor, 1997]. In other words, moving from fault center to tip represents decreasing time for topographic growth. Our results suggest that lateral fault growth is not a continuous process and that care must be taken when making that assumption; the space-for-time substitution may only be valid at the earlier stages of deformation (e.g., initial ~3–4 Myr for the Pine Forest Range). At the catchment scale, channel knickpoint migration velocities in tectonically active environments can be related to uplift rate [Niemann *et al.*, 2001; Attal *et al.*, 2008; Whittaker, 2012], such that knickpoint elevations should mimic a displacement profile consistent with the tip propagation model (Figure 2a [Whittaker, 2012]). In the Pine Forest Range, where the thermochronometer data show that fault lengthening may have ceased by ~8 Ma, knickpoint height is rather uniform across the range [Ellis *et al.*, 2015]; this mimics, instead, a displacement profile more consistent with the constant fault-length model (Figure 2c). In conclusion, observed spatial patterns of Pine Forest Range fluvial knickpoints also support the thermochronologic evidence that shows that fault development best aligns with the constant fault-length model.

6.6. Guidance for Future Research

Quantifying fault slip histories is subject to many limitations. Fault movement is often inferred from uplifted footwall terraces [Jackson and McKenzie, 1983; Morewood and Roberts, 1999] or from syn-sedimentary fill in the hanging walls [Morley, 1999; Contreras *et al.*, 2000]. However, accurate measures of fault throw from the sedimentary fill of the hanging wall are only truly possible when sedimentation rates exceed fault displacement rates, thus preserving the fault displacement history. As we have shown, even displacement or tip propagation rate estimates are limited by the accuracy of age determinations. This study is one of the first, to our knowledge, to explore the fidelity to which AHe data can be used to calculate a lateral fault propagation rate and hence test conceptual models for normal fault growth [see also Krugh, 2008]. We contend that low-temperature thermochronology remains an underutilized tool for addressing the three-dimensional aspects of fault evolution. As general rules of thumb, we recommend that the apatite (U-Th)/He system will be particularly useful in areas where the following criteria are met: (a) widespread plutonism or exposure of other favorable lithologies that provide high-quality grains necessary for analysis, (b) sufficient exhumation exposes a suite of paleodepths that span from within to below the fossil PRZ/PAZ (~2–5 km depth in most settings), (c) intact pre-faulting stratigraphy or an equivalent datum exists to estimate paleodepth and footwall tilting, and (d) the fault is long enough (>~30 km) to allow adequate distance between transects. We recommend that at least three sample transects containing ≥ 4 samples are collected (a) perpendicular to the fault trace and (b) at sufficient along-strike distances to reduce the possibility for overlapping age uncertainties. This separation distance should be based on cooling age uncertainties that will vary with the specific thermochronometer system used (e.g., AHe or AFT) and crystallography (i.e., grain size, morphology, purity, and radiation damage). For example, cooling age uncertainties for AHe are ~6–10% and for AFT are ~15–20% [Ehlers and Farley, 2003]. Apatite $^4\text{He}/^3\text{He}$ thermochronometry provides even lower-temperature sensitivity and hence may also be an approach worth considering [Colgan *et al.*, 2008; Schildgen *et al.*, 2010]. In general, the age range for the onset of rapid cooling is minimized by an order of magnitude decrease in uncertainty when multiple thermochronometers are utilized. Thus, there remains great potential in combining these systems to further investigate the evolution of upper crustal deformation.

7. Conclusions

Growth of the Pine Forest Range frontal fault in the Nevada Basin and Range is most consistent with the constant fault-length model for fault growth. Thermochronologic data show that within uncertainties, fault-driven rapid cooling commenced concomitantly at all sample locations along strike between approximately 15 and 11 Ma, reached its modern fault length within ~3–4 Myr (~10–9 Ma), and has continued to slip with negligible lengthening since ~8 Ma. We speculate that cessation of lengthening may be due to interaction with nearby fault segments, confrontation of an unknown barrier, exploitation of preexisting structures, and/or variation in crustal mechanical properties. Results from a single transect in the adjacent Jackson Mountains show that rapid exhumation was ongoing by ~13 Ma at a rate of ~0.3 km/Myr and illustrates the shortcomings of a single sample transect in evaluating the spatiotemporal evolution of the range-bounding fault. Overall, our results suggest that modern Basin and Range physiography was established by the middle to late Miocene, that the constant-length model for fault growth may be more accurate to describe crustal-scale normal faults, and imply that the connection between fault-driven landscapes and their tectonic boundary conditions may be more limited than previously thought. Most information on the spatiotemporal patterns of fault-driven exhumation come from combining (a) multiple thermochronometer analyses on each sample, (b) several elevation transects that span a significant along-strike distance, and (c) robust interpretation techniques such as thermal history modeling and regression analysis. We hope that this study helps establish a framework for using low-temperature thermochronology to address increasingly complex questions about how faults grow.

Acknowledgments

M. Curry thanks the UNC Department of Geological Sciences Martin Fund, John Rogers and the Rogers Fund, GSA, and Sigma Xi for their financial support. Julia Ellis and Jim Mize provided valuable assistance in the field and James Metcalf lent crucial help in the lab with the AHe analyses. We thank Kevin Stewart, Rich Ketcham, Mike Diggles, and Scott Minor for their assistance and thoughtful comments. We also acknowledge Associate Editor Sean Long and Editor John Geissman for their work. Thoughtful reviews by Andy Nicol, Jim Faulds, and two anonymous reviewers greatly improved this manuscript. Any use of trade, product, or firm names is for descriptive purposes only and does not imply endorsement by the U.S. Government. The data used in this paper are available in Tables 1 and 2, the supporting information file, and cited references.

References

- Amos, C. B., D. W. Burbank, and S. A. L. Read (2010), Along-strike growth of the Ostler Fault, New Zealand: Consequences for drainage deflection above active thrusts, *Tectonics*, 29, TC4021, doi:10.1029/2009TC002613.
- Ascione, A., S. Mazzoli, P. Petrosino, and E. Valente (2013), A decoupled kinematic model for active normal faults: Insights from the 1980, $M_s = 6.9$ Irpinia earthquake, southern Italy, *Geol. Soc. Am. Bull.*, 125(7–8), 1239–1259, doi:10.1130/b30814.1.
- Attal, M., G. E. Tucker, A. C. Whittaker, P. A. Cowie, and G. P. Roberts (2008), Modeling fluvial incision and transient landscape evolution: Influence of dynamic channel adjustment, *J. Geophys. Res.*, 113, F03013, doi:10.1029/2007JF000893.
- Balestrieri, M. L., M. Bernet, M. T. Brandon, V. Picotti, P. Reiners, and M. Zattin (2003), Pliocene and Pleistocene exhumation and uplift of two key areas of the northern Apennines, *Quat. Int.*, 101–102, 67–73, doi:10.1016/S1040-6182(02)00089-7.
- Barnes, J. B., T. A. Ehlers, N. McQuarrie, P. B. O'Sullivan, and S. Tawackoli (2008), Thermochronometer record of central Andean Plateau growth, Bolivia (19.5°S), *Tectonics*, 27, TC3003, doi:10.1029/2007TC002174.
- Barnes, J. B., A. L. Densmore, M. Mukul, R. Sinha, V. Jain, and S. K. Tandon (2011), Interplay between faulting and base level in the development of Himalayan frontal fold topography, *J. Geophys. Res.*, 116, F03012, doi:10.1029/2010JF001841.
- Bennett, E., J. Youngson, J. Jackson, R. Norris, G. M. Raisbeck, and F. You (2006), Combining geomorphic observations with in situ cosmogenic isotope measurements to study anticline growth and fault propagation in Central Otago, New Zealand, *N. Z. J. Geol. Geophys.*, 49, 15, doi:10.1080/00288306.2006.9515161.
- Bennett, E. R., J. H. Youngson, J. A. Jackson, R. J. Norris, G. M. Raisbeck, F. You, and E. Fielding (2005), Growth of South Rough Ridge, central Otago, New Zealand: Using in situ cosmogenic isotopes and geomorphology to study an active, blind reverse fault, *J. Geophys. Res.*, 110, B02404, doi:10.1029/2004JB003184.
- Blackwell, D. D., and M. Richards (2004), Geothermal map of North America, AAPG Map 423, scale 1:6,500,000.
- Brichau, S., U. Ring, R. A. Ketcham, A. Carter, D. Stockli, and M. Brunel (2006), Constraining the long-term evolution of the slip rate for a major extensional fault system in the central Aegean, Greece, using thermochronology, *Earth Planet. Sci. Lett.*, 241(1–2), 293–306, doi:10.1016/j.epsl.2005.09.065.
- Brueseke, M., W. Hart, and M. Heizler (2008), Diverse mid-Miocene silicic volcanism associated with the Yellowstone–Newberry thermal anomaly, *Bull. Volcanol.*, 70(3), 343–360, doi:10.1007/s00445-007-0142-5.
- Camp, V. E., M. E. Ross, R. A. Duncan, N. A. Jarboe, R. S. Coe, B. B. Hanan, and J. A. Johnson (2013), The Steens Basalt: Earliest lavas of the Columbia River Basalt Group, *Geol. Soc. Am. Spec. Pap.*, 497, 87–116, doi:10.1130/2013.2497(04).
- Cartwright, J. A., B. D. Trudgill, and C. S. Mansfield (1995), Fault growth by segment linkage—An explanation for scatter in maximum displacement and trace length data from the Canyonlands Grabens of SE Utah, *J. Struct. Geol.*, 17(9), 1319–1326, doi:10.1016/0191-8141(95)00033-a.
- Castor, S. B., and C. D. Henry (2000), Geology, geochemistry, and origin of volcanic rock-hosted uranium deposits in northwestern Nevada and southeastern Oregon, USA, *Ore Geol. Rev.*, 16(1–2), 1–40, doi:10.1016/S0169-1368(99)00021-9.
- Childs, C., A. Nicol, J. J. Walsh, and J. Watterson (2003), The growth and propagation of syndimentary faults, *J. Struct. Geol.*, 25(4), 633–648, doi:10.1016/S0191-8141(02)00054-8.
- Clark, R. M., and S. J. D. Cox (1996), A modern regression approach to determining fault displacement-length scaling relationships, *J. Struct. Geol.*, 18(2–3), 147–152, doi:10.1016/S0191-8141(96)80040-x.
- Colgan, J. P., and C. D. Henry (2009), Rapid middle Miocene collapse of the Mesozoic orogenic plateau in north-central Nevada, *Int. Geol. Rev.*, 51(9–11), 920–961, doi:10.1080/00206810903056731.
- Colgan, J. P., T. A. Dumitru, P. W. Reiners, J. L. Wooden, and E. L. Miller (2006a), Cenozoic tectonic evolution of the Basin and Range Province in northwestern Nevada, *Am. J. Sci.*, 306(8), 616–654, doi:10.2475/08.2006.02.
- Colgan, J. P., T. A. Dumitru, M. McWilliams, and E. L. Miller (2006b), Timing of Cenozoic volcanism and Basin and Range extension in northwestern Nevada: New constraints from the northern Pine Forest Range, *Geol. Soc. Am. Bull.*, 118(1–2), 126–139, doi:10.1130/b25681.1.
- Colgan, J. P., D. L. Shuster, and P. W. Reiners (2008), Two-phase Neogene extension in the northwestern Basin and Range recorded in a single thermochronology sample, *Geology*, 36(8), 631–634, doi:10.1130/g24897a.

- Contreras, J., M. H. Anders, and C. H. Scholz (2000), Growth of a normal fault system: Observations from the Lake Malawi basin of the east African rift, *J. Struct. Geol.*, *22*(2), 159–168, doi:10.1016/S0191-8141(99)00157-1.
- Coolbaugh, M., et al. (2005), Geothermal potential map of the Great Basin, western United States, Nevada Bureau of Mines and Geology Map 151, scale 1:1,000,000, Reno, Nev.
- Cowie, P. A. (1998), A healing–reloading feedback control on the growth rate of seismogenic faults, *J. Struct. Geol.*, *20*(8), 1075–1087, doi:10.1016/S0191-8141(98)00034-0.
- Cowie, P. A., and C. H. Scholz (1992a), Displacement-length scaling relationship for faults: Data synthesis and discussion, *J. Struct. Geol.*, *14*(10), 1149–1156, doi:10.1016/0191-8141(92)90066-6.
- Cowie, P. A., and C. H. Scholz (1992b), Growth of faults by accumulation of seismic slip, *J. Geophys. Res.*, *97*, 11,085–11,095, doi:10.1029/92JB00586.
- Cowie, P. A., and C. H. Scholz (1992c), Physical explanation for the displacement-length relationship of faults using a post-yield fracture mechanics model, *J. Struct. Geol.*, *14*(10), 1133–1148, doi:10.1016/0191-8141(92)90065-5.
- Cowie, P. A., S. Gupta, and N. H. Dawers (2000), Implications of fault array evolution for synrift depocentre development: Insights from a numerical fault growth model, *Basin Res.*, *12*(3–4), 241–261, doi:10.1111/j.1365-2117.2000.00126.x.
- Davarpanah, A., and H. A. Babaie (2013), Anisotropy of fractal dimension of normal faults in northern Rocky Mountains: Implications for the kinematics of Cenozoic extension and Yellowstone hotspot's thermal expansion, *Tectonophysics*, *608*, 530–544, doi:10.1016/j.tecto.2013.08.031.
- Dawers, N. H., M. H. Anders, and C. H. Scholz (1993), Growth of normal faults: Displacement-length scaling, *Geology*, *21*(12), 1107–1110, doi:10.1130/0091-7613(1993)021<1107:gonfdl>2.3.co;2.
- Densmore, A. L., N. H. Dawers, S. Gupta, R. Guidon, and T. Goldin (2004), Footwall topographic development during continental extension, *J. Geophys. Res.*, *109*, F03001, doi:10.1029/2003JF000115.
- Densmore, A. L., P. A. Allen, and G. Simpson (2007a), Development and response of a coupled catchment fan system under changing tectonic and climatic forcing, *J. Geophys. Res.*, *112*, F01002, doi:10.1029/2006JF000474.
- Densmore, A. L., S. Gupta, P. A. Allen, and N. H. Dawers (2007b), Transient landscapes at fault tips, *J. Geophys. Res.*, *112*, F03S08, doi:10.1029/2006JF000560.
- Dodson, M. H. (1973), Closure temperature in cooling geochronological and petrological systems, *Contrib. Mineral. Petrol.*, *40*(3), 259–274, doi:10.1007/BF00373790.
- Dugdale, D. S. (1960), Yielding of steel sheets containing slits, *J. Mech. Phys. Solids*, *8*(2), 100–104, doi:10.1016/0022-5096(60)90013-2.
- Dumitru, T. A. (2000), Fission-track geochronology, in *Quaternary Geochronology: Methods and Applications*, AGU Ref. Shelf, edited by J. S. Noller, J. M. Sowers, and W. R. Lettis, pp. 131–155, AGU, Washington, D. C.
- Egger, A. E., J. M. G. Glen, and D. K. McPhee (2014), Structural controls on geothermal circulation in Surprise Valley, California: A re-evaluation of the Lake City fault zone, *Geol. Soc. Am. Bull.*, *126*(3–4), 523–531, doi:10.1130/b30785.1.
- Ehlers, T. A. (2005), Crustal thermal processes and the interpretation of thermochronometer data, in *Low-Temperature Thermochronology: Techniques, Interpretations, and Applications*, *Rev. in Mineral. & Geochem.*, vol. 58, edited by P. W. Reiners and T. A. Ehlers, pp. 315–350, Mineral. Soc. of Am., Chantilly, Va.
- Ehlers, T. A., and K. A. Farley (2003), Apatite (U-Th)/He thermochronometry; methods and applications to problems in tectonic and surface processes, *Earth Planet. Sci. Lett.*, *206*(1–2), 1–14, doi:10.1016/S0012-821X(02)01069-5.
- Ellis, M. A., J. B. Barnes, and J. P. Colgan (2015), Geomorphic evidence for enhanced Pliocene–Quaternary faulting in the northwestern Basin and Range, *Lithosphere*, *7*(1), 59–72, doi:10.1130/L401.1.
- Farley, K. A. (2000), Helium diffusion from apatite; general behavior as illustrated by Durango fluorapatite, *J. Geophys. Res.*, *105*, 2903–2914, doi:10.1029/1999JB900348.
- Farley, K. A. (2002), (U-Th)/He dating: Techniques, calibrations, and applications, in *Noble Gases in Geochemistry and Cosmochemistry*, *Rev. in Mineral. and Geochem.*, vol. 47, edited by D. Porcelli, C. J. Ballentine, and R. Wieler, pp. 819–843, Mineral. Soc. of Am., Washington, D. C.
- Faulds, J. E., and N. H. Hinz (2015), Favorable tectonic and structural settings of geothermal systems in the Great Basin region, western USA: Proxies for discovering blind geothermal systems: Proceedings World Geothermal Congress, p. 6, Melbourne, Australia, 19–25 April 2015.
- Faulds, J. E., C. D. Henry, and N. H. Hinz (2005), Kinematics of the northern Walker Lane: An incipient transform fault along the Pacific-North American plate boundary, *Geology*, *33*(6), 505–508, doi:10.1130/G21274.1.
- Fitzgerald, P. G., and A. J. W. Gleadow (1990), New approaches in fission track geochronology as a tectonic tool: Examples from the Transantarctic Mountains, *Int. J. Radiat. Appl. Instrum., Part D Nucl. Tracks Radiat. Meas.*, *17*(3), 351–357, doi:10.1016/1359-0189(90)90057-5.
- Fitzgerald, P. G., J. E. Fryxell, and B. P. Wernicke (1991), Miocene crustal extension and uplift in southeastern Nevada; constraints from fission track analysis, *Geology*, *19*(10), 1013–1016, doi:10.1130/0091-7613(1991)019<1013:MCEAU>2.3.CO;2.
- Fitzgerald, P. G., S. L. Baldwin, L. E. Webb, and P. O'Sullivan (2006), (U-Th)/He data from slowly cooled crustal terranes and the interpretation of intra-sample variations of single crystal apatite ages from vertical profiles, *Chem. Geol.*, *225*, 91–120, doi:10.1016/j.chemgeo.2005.09.001.
- Flowers, R. M., B. P. Wernicke, and K. A. Farley (2008), Unroofing, incision, and uplift history of the southwestern Colorado Plateau from apatite (U-Th)/He thermochronometry, *Geol. Soc. Am. Bull.*, *120*(5–6), 571–587, doi:10.1130/B26231.1.
- Flowers, R. M., R. A. Ketcham, D. L. Shuster, and K. A. Farley (2009), Apatite (U-Th)/He thermochronometry using a radiation damage accumulation and annealing model, *Geochim. Cosmochim. Acta*, *73*(8), 2347–2365, doi:10.1016/j.gca.2009.01.015.
- Fosdick, J. C., and J. P. Colgan (2008), Miocene extension in the East Range, Nevada: A two-stage history of normal faulting in the northern Basin and Range, *Geol. Soc. Am. Bull.*, *120*(9–10), 1198–1213, doi:10.1130/b26201.1.
- Foster, D. A., D. S. Miller, and C. F. Miller (1991), Tertiary extension in the Old Woman Mountains area, California: Evidence from apatite fission-track analysis, *Tectonics*, *10*, 875–886, doi:10.1029/91TC00865.
- Gawthorpe, R. L., C. A. L. Jackson, M. J. Young, I. R. Sharp, A. R. Moustafa, and C. W. Leppard (2003), Normal fault growth, displacement localisation and the evolution of normal fault populations: The Hammam Faraun fault block, Suez rift, Egypt, *J. Struct. Geol.*, *25*(6), 883–895, doi:10.1016/S0191-8141(02)00088-3.
- Gillespie, P. A., J. J. Walsh, and J. Watterson (1992), Limitations of dimension and displacement data from single faults and the consequences for data analysis and interpretation, *J. Struct. Geol.*, *14*(10), 1157–1172, doi:10.1016/0191-8141(92)90067-7.
- Green, P. F., I. R. Duddy, A. J. W. Gleadow, P. R. Tingate, and G. M. Laslett (1986), Thermal annealing of fission tracks in apatite; 1. A qualitative description, *Chem. Geol. Isot. Geosci. Sect.*, *59*(4), 237–253, doi:10.1016/0168-9622(86)90074-6.
- Green, P. F., I. R. Duddy, G. M. Laslett, K. A. Hegarty, A. J. W. Gleadow, and J. F. Lovering (1989), Thermal annealing of fission tracks in apatite; 4. Quantitative modelling techniques and extension to geological timescales, *Chem. Geol. Isot. Geosci. Sect.*, *79*(2), 155–182, doi:10.1016/0168-9622(89)90018-3.

- Gudmundsson, A. (2004), Effects of Young's modulus on fault displacement, *C. R. Geosci.*, 336(1), 85–92, doi:10.1016/j.crte.2003.09.018.
- Gupta, A., and C. H. Scholz (2000), A model of normal fault interaction based on observations and theory, *J. Struct. Geol.*, 22(7), 865–879, doi:10.1016/S0191-8141(00)00011-0.
- Harbor, D. J. (1997), Landscape evolution at the margin of the Basin and Range, *Geology*, 25(12), 1111–1114, doi:10.1130/0091-7613(1997)025<1111:leatmo>2.3.co;2.
- Harrison, T. M., and P. K. Zeitler (2005), Fundamentals of noble gas thermochronometry, *Rev. Mineral. Geochem.*, 58(1), 123–149, doi:10.2138/rmg.2005.58.5.
- Henry, C. D., and M. E. Perkins (2001), Sierra Nevada–Basin and Range transition near Reno, Nevada: Two-stage development at 12 and 3 Ma, *Geology*, 29(8), 719–722, doi:10.1130/0091-7613(2001)029<0719:snbart>2.0.co;2.
- Jackson, C. A. L., D. T. Carruthers, S. N. Mahlo, and O. Briggs (2014), Can polygonal faults help locate deep-water reservoirs? *Am. Assoc. Pet. Geol. Bull.*, 98(9), 1717–1738, doi:10.1306/03131413104.
- Jackson, J., and D. McKenzie (1983), The geometrical evolution of normal-fault systems, *J. Struct. Geol.*, 5(5), 471–482, doi:10.1016/0191-8141(83)90053-6.
- Jackson, J. A., and N. J. White (1989), Normal faulting in the upper continental crust: Observations from regions of active extension, *J. Struct. Geol.*, 11(1–2), 15–36, doi:10.1016/0191-8141(89)90033-3.
- Ketcham, R. A. (2005), Forward and inverse modeling of low-temperature thermochronometry data, in *Low-Temperature Thermochronology: Techniques, Interpretations, and Applications*, vol. 58, edited by P. W. Reiners and T. A. Ehlers, pp. 275–314, Mineral. Soc. of Am., Chantilly, Va.
- Ketcham, R. A. (2016), Hefty, version 1.9.1, Apatite to Zircon, Inc. and Richard Ketcham.
- Ketcham, R. A., C. Gautheron, and L. Tassan-Got (2011), Accounting for long alpha-particle stopping distances in (U-Th-Sm)/He geochronology: Refinement of the baseline case, *Geochim. Cosmochim. Acta*, 75(24), 7779–7791, doi:10.1016/j.gca.2011.10.011.
- Kim, Y. S., and D. J. Sanderson (2005), The relationship between displacement and length of faults: A review, *Earth Sci. Rev.*, 68(3–4), 317–334, doi:10.1016/j.earscirev.2004.06.003.
- Kim, Y.-S., J.-H. Kihm, and K. Jin (2011), Interpretation of the rupture history of a low slip-rate active fault by analysis of progressive displacement accumulation: An example from the Quaternary Eupcheon Fault, SE Korea, *J. Geol. Soc. London*, 168(1), 273–288, doi:10.1144/0016-76492010-088.
- King, G. C. P., R. S. Stein, and J. B. Rundle (1988), The growth of geological structures by repeated earthquakes. Part 1: Conceptual framework, *J. Geophys. Res.*, 93, 13,307–13,318, doi:10.1029/JB093iB11p13307.
- Krantz, R. W. (1988), Multiple fault sets and three-dimensional strain: Theory and application, *J. Struct. Geol.*, 10(3), 225–237, doi:10.1016/0191-8141(88)90056-9.
- Krugh, W. C. (2008), Low-temperature thermochronologic constraints on fault array evolution and patterns of range-scale denudation, PhD thesis, ETH Zurich, Zurich, Switzerland.
- Lerch, D. W., E. Miller, M. McWilliams, and J. Colgan (2008), Tectonic and magmatic evolution of the northwestern Basin and Range and its transition to unextended volcanic plateaus: Black Rock Range, Nevada, *Geol. Soc. Am. Bull.*, 120(3–4), 300–311, doi:10.1130/b26151.1.
- Lin, J., and E. M. Parmentier (1988), Quasistatic propagation of a normal fault: A fracture mechanics model, *J. Struct. Geol.*, 10(3), 249–262, doi:10.1016/0191-8141(88)90058-2.
- Maher, K. A. (1989), Geology of the Jackson Mountains, northwest Nevada, PhD Thesis, Calif. Inst. of Technol., Pasadena.
- Manighetti, I., G. C. P. King, Y. Gaudemer, C. H. Scholz, and C. Doubre (2001), Slip accumulation and lateral propagation of active normal faults in Afar, *J. Geophys. Res.*, 106, 13,667–13,696, doi:10.1029/2000JB900471.
- Martin, A. J., S. J. Wyld, J. E. Wright, and J. H. Bradford (2010), The Lower Cretaceous King Lear Formation, northwest Nevada: Implications for Mesozoic orogenesis in the western U.S. Cordillera, *Geol. Soc. Am. Bull.*, 122(3/4), 537–562, doi:10.1130/b26555.1.
- McGrath, A. (1992), Fault propagation and growth: A study of the Triassic and Jurassic from Watchet and Kilve, North Somerset, MSc Thesis, R. Holloway and Bedford New Coll., The Univ. of London, London, England.
- McLeod, A. E., N. H. Dawers, and J. R. Underhill (2000), The propagation and linkage of normal faults: Insights from the Strathspey–Brent–Statfjord fault array, northern North Sea, *Basin Res.*, 12(3–4), 263–284, doi:10.1111/j.1365-2117.2000.00124.x.
- Medwedeff, D. A. (1992), Geometry and kinematics of an active, laterally propagating wedge thrust, Wheeler Ridge, California, in *Structural Geology of Fold and Thrust Belts*, edited by S. Mitra and G. W. Fisher, pp. 3–28, Johns Hopkins Univ. Press, Baltimore, Md.
- Meyer, V., A. Nicol, C. Childs, J. J. Walsh, and J. Watterson (2002), Progressive localisation of strain during the evolution of a normal fault population, *J. Struct. Geol.*, 24(8), 1215–1231, doi:10.1016/S0191-8141(01)00104-3.
- Miller, E. L., T. A. Dumitru, R. W. Brown, and P. B. Gans (1999), Rapid Miocene slip on the Snake Range–Deep Creek Range fault system, east-central Nevada, *Geol. Soc. Am. Bull.*, 111(6), 886–905, doi:10.1130/0016-7606(1999)111<0886:RMSOTS>2.3.CO;2.
- Morewood, N. C., and G. P. Roberts (1999), Lateral propagation of the surface trace of the South Alkyonides normal fault segment, central Greece: Its impact on models of fault growth and displacement-length relationships, *J. Struct. Geol.*, 21(6), 635–652, doi:10.1016/S0191-8141(99)00049-8.
- Morewood, N. C., and G. P. Roberts (2002), Surface observations of active normal fault propagation: Implications for growth, *J. Geol. Soc. London*, 159(3), 263–272, doi:10.1144/0016-764901-046.
- Morley, C. K. (1999), Patterns of displacement along large normal faults: Implications for basin evolution and fault propagation, based on examples from east Africa, *Am. Assoc. Pet. Geol. Bull.*, 83(4), 613–634.
- Mouslopoulou, V., J. J. Walsh, and A. Nicol (2009), Fault displacement rates on a range of timescales, *Earth Planet. Sci. Lett.*, 278(3–4), 186–197, doi:10.1016/j.epsl.2008.11.031.
- Mouslopoulou, V., A. Nicol, J. J. Walsh, J. G. Begg, D. B. Townsend, and D. T. Hristopulos (2012), Fault-slip accumulation in an active rift over thousands to millions of years and the importance of paleoearthquake sampling, *J. Struct. Geol.*, 36, 71–80, doi:10.1016/j.jsg.2011.11.010.
- Muraoka, H., and H. Kamata (1983), Displacement distribution along minor fault traces, *J. Struct. Geol.*, 5(5), 483–495, doi:10.1016/0191-8141(83)90054-8.
- Nahm, A. L., T. Öhman, and D. A. Kring (2013), Normal faulting origin for the Cordillera and Outer Rook Rings of Orientale Basin, the Moon, *J. Geophys. Res. Planets*, 118, 190–205, doi:10.1002/jgre.20045.
- Nicol, A., J. Watterson, J. J. Walsh, and C. Childs (1996), The shapes, major axis orientations and displacement patterns of fault surfaces, *J. Struct. Geol.*, 18(2–3), 235–248, doi:10.1016/S0191-8141(96)80047-2.
- Nicol, A., J. J. Walsh, T. Manzocchi, and N. Morewood (2005), Displacement rates and average earthquake recurrence intervals on normal faults, *J. Struct. Geol.*, 27(3), 541–551, doi:10.1016/j.jsg.2004.10.009.
- Nicol, A., C. Childs, J. J. Walsh, T. Manzocchi, and M. P. J. Schöpfer (2016), Interactions and growth of faults in an outcrop-scale system, in *The Geometry and Growth of Normal Faults, Spec. Publ.*, vol. 439, edited by C. Childs et al., pp. 1–17, Geol. Soc., London.

- Niemann, J. D., N. M. Gasparini, G. E. Tucker, and R. L. Bras (2001), A quantitative evaluation of Playfair's law and its use in testing long-term stream erosion models, *Earth Surf. Processes Landforms*, 26(12), 1317–1332, doi:10.1002/esp.272.
- Opheim, J. A., and A. Gudmundsson (1989), Formation and geometry of fractures, and related volcanism, of the Krafla fissure swarm, northeast Iceland, *Geol. Soc. Am. Bull.*, 101(12), 1608–1622, doi:10.1130/0016-7606(1989)101<1608:FAGOFA>2.3.CO;2.
- Peacock, D. C. P., and D. J. Sanderson (1991), Displacements, segment linkage and relay ramps in normal fault zones, *J. Struct. Geol.*, 13(6), 721–733, doi:10.1016/0191-8141(91)90033-F.
- Polit, A. T., R. A. Schultz, and R. Soliva (2009), Geometry, displacement–length scaling, and extensional strain of normal faults on Mars with inferences on mechanical stratigraphy of the Martian crust, *J. Struct. Geol.*, 31(7), 662–673, doi:10.1016/j.jsg.2009.03.016.
- Quinn, M. J., J. E. Wright, and S. J. Wyld (1997), Happy Creek igneous complex and tectonic evolution of the early Mesozoic arc in the Jackson Mountains, northwest Nevada, *Geol. Soc. Am. Bull.*, 109(4), 461–482, doi:10.1130/0016-7606(1997)109<0461:hccat>2.3.co;2.
- Reiners, P. W., T. A. Ehlers, P. K. Zeitler, and J. J. Rosso (2005), Past, present, and future of thermochronology, in *Low-Temperature Thermochronology: Techniques, Interpretations, and Applications*, Rev. in Mineral. & Geochem., vol. 58, edited by P. W. Reiners and T. A. Ehlers, pp. 1–18, Mineral. Soc. of Am., Chantilly, Va.
- Ring, U., M. T. Brandon, S. D. Willett, and G. S. Lister (1999), Exhumation processes, in *Exhumation Processes; Normal Faulting, Ductile Flow and Erosion*, Spec. Publ., vol. 154, edited by U. Ring et al., pp. 1–27, Geol. Soc. of London, London.
- Saltus, R. W., and R. C. Jachens (1995), Gravity and basin-depth maps of the Basin and Range Province, western United States, U.S. Geological Survey Geophysical Investigations Map GP-1012, scale 1:2,500,000, Reston, Va.
- Schildgen, T. F., G. Balco, and D. L. Shuster (2010), Canyon incision and knickpoint propagation recorded by apatite ⁴He/³He thermochronometry, *Earth Planet. Sci. Lett.*, 293(3–4), 377–387, doi:10.1016/j.epsl.2010.03.009.
- Schlagenhauf, A., I. Manighetti, J. Malavieille, and S. Dominguez (2008), Incremental growth of normal faults: Insights from a laser-equipped analog experiment, *Earth Planet. Sci. Lett.*, 273(3–4), 299–311, doi:10.1016/j.epsl.2008.06.042.
- Schlische, R. W., S. S. Young, R. V. Ackermann, and A. Gupta (1996), Geometry and scaling relations of a population of very small rift-related normal faults, *Geology*, 24(8), 683–686, doi:10.1130/0091-7613(1996)024<0683:gasroa>2.3.co;2.
- Scholz, C. H. (2002), *The Mechanics of Earthquakes and Faulting*, 2nd ed., Cambridge Univ. Press, Cambridge, U. K.
- Scholz, C. H., and J. C. Contreras (1998), Mechanics of continental rift architecture, *Geology*, 26(11), 967–970, doi:10.1130/0091-7613(1998)026<0967:mocra>2.3.co;2.
- Scholz, C. H., and P. A. Cowie (1990), Determination of the total strain from faulting using slip measurements, *Nature*, 346(6287), 837–839, doi:10.1038/346837a0.
- Shuster, D. L., and K. A. Farley (2009), The influence of artificial radiation damage and thermal annealing on helium diffusion kinetics in apatite, *Geochim. Cosmochim. Acta*, 73(1), 183–196, doi:10.1016/j.gca.2008.10.013.
- Shuster, D. L., R. M. Flowers, and K. A. Farley (2006), The influence of natural radiation damage on helium diffusion kinetics in apatite, *Earth Planet. Sci. Lett.*, 249(3–4), 148–161, doi:10.1016/j.epsl.2006.07.028.
- Smith, J. G. (1973), Map of the Duffer Peak Quadrangle, Humboldt County, Nevada, U.S. Geol. Surv. Misc. Geol. Investig. Map I-606, scale 1:48,000, Washington, D. C.
- Snow, J. K., and B. Wernicke (2000), Cenozoic tectonism in the central Basin and Range; magnitude, rate, and distribution of upper crustal strain, *Am. J. Sci.*, 300(9), 659–719, doi:10.2475/ajs.300.9.659.
- Sobel, E. R., M. Oskin, D. Burbank, and A. Mikolaichuk (2006), Exhumation of basement-cored uplifts; example of the Kyrgyz Range quantified with apatite fission track thermochronology, *Tectonics*, 25, TC2008, doi:10.1029/2005TC001809.
- Soliva, R., A. Benedicto, R. A. Schultz, L. Maerten, and L. Micarelli (2008), Displacement and interaction of normal fault segments branched at depth: Implications for fault growth and potential earthquake rupture size, *J. Struct. Geol.*, 30(10), 1288–1299, doi:10.1016/j.jsg.2008.07.005.
- Spotila, J. A. (2005), Applications of low-temperature thermochronometry to quantification of recent exhumation in mountain belts, *Rev. Mineral. Geochem.*, 58(1), 449–466, doi:10.2138/rmg.2005.58.17.
- Stockli, D. F. (1999), Regional timing and spatial distribution of Miocene extension in the northern Basin and Range Province, PhD thesis, Stanford Univ., Stanford, Calif.
- Stockli, D. F. (2005), Application of low-temperature thermochronometry to extensional tectonic settings, in *Low-Temperature Thermochronology: Techniques, Interpretations, & Applications*, Rev. in Mineral. & Geochem., vol. 58, edited by P. W. Reiners and T. A. Ehlers, pp. 441–448, Mineral. Soc. of Am., Chantilly, Va.
- Stockli, D. F., B. E. Surpless, T. A. Dumitru, and K. Farley (2002), Thermochronological constraints on the timing and magnitude of Miocene and Pliocene extension in the central Wassuk Range, western Nevada, *Tectonics*, 21(4), 1028, doi:10.1029/2001TC001295.
- Stockli, D. F., T. A. Dumitru, M. O. McWilliams, and K. A. Farley (2003), Cenozoic tectonic evolution of the White Mountains, California and Nevada, *Geol. Soc. Am. Bull.*, 115(7), 788–816, doi:10.1130/0016-7606(2003)115<0788:ctootw>2.0.co;2.
- Strachan, L. J., F. Rarity, R. L. Gawthorpe, P. Wilson, I. Sharp, and D. Hodgetts (2013), Submarine slope processes in rift-margin basins, Miocene Suez Rift, Egypt, *Geol. Soc. Am. Bull.*, 125(1–2), 109–127, doi:10.1130/b30665.1.
- Trexler, J. H., P. H. Cashman, C. D. Henry, T. Muntean, K. Schwartz, A. Tenbrink, J. E. Faults, M. Perkins, and T. Kelly (2000), Neogene basins in western Nevada document the tectonic history of the Sierra Nevada–Basin and Range transition zone for the last 12 Ma, in *Great Basin and Sierra Nevada, Field Guide 2*, edited by D. R. Lageson, S. G. Peters, and M. M. Lahren, pp. 97–116, Geol. Soc. of Am., Boulder, Colo.
- Villemin, T., J. Angelier, and V. Sunwoo (1995), Fractal distribution of fault length and offsets: Implications of brittle deformation evaluation—Lorraine Coal Basin, in *Fractals in the Earth Sciences*, edited by C. C. Barton and P. R. LaPointe, pp. 205–226, Plenum, New York.
- Walsh, J. J., and J. Watterson (1987), Distributions of cumulative displacement and seismic slip on a single normal fault surface, *J. Struct. Geol.*, 9(8), 1039–1046, doi:10.1016/0191-8141(87)90012-5.
- Walsh, J. J., and J. Watterson (1988), Analysis of the relationship between displacements and dimensions of faults, *J. Struct. Geol.*, 10(3), 239–247, doi:10.1016/0191-8141(88)90057-0.
- Walsh, J. J., A. Nicol, and C. Childs (2002), An alternative model for the growth of faults, *J. Struct. Geol.*, 24(11), 1669–1675, doi:10.1016/S0191-8141(01)00165-1.
- Walsh, J. J., W. R. Bailey, C. Childs, A. Nicol, and C. G. Bonson (2003), Formation of segmented normal faults: A 3-D perspective, *J. Struct. Geol.*, 25(8), 1251–1262, doi:10.1016/S0191-8141(02)00161-X.
- Watts, A. B., and E. B. Burrov (2003), Lithospheric strength and its relationship to the elastic and seismogenic layer thickness, *Earth Planet. Sci. Lett.*, 213(1–2), 113–131, doi:10.1016/S0012-821X(03)00289-9.
- Wells, D. L., and K. J. Coppersmith (1994), New empirical relationships among magnitude, rupture length, rupture width, rupture area, and surface displacement, *Bull. Seismol. Soc. Am.*, 84(4), 974–1002.

- Wernicke, B. (1992), Cenozoic extensional tectonics of the U.S. Cordillera, in *The Cordilleran Orogen; Coterminal U.S.*, edited by B. C. Burchfiel, P. W. Lipman, and M. D. Zoback, pp. 553–581, Geol. Soc. of Am., Boulder, Colo.
- Whittaker, A. C. (2012), How do landscapes record tectonics and climate?, *Lithosphere*, 4(2), 160–164, doi:10.1130/rlf.l003.1.
- Wilkins, S. J., and M. J. Gross (2002), Normal fault growth in layered rocks at Split Mountain, Utah: Influence of mechanical stratigraphy on dip linkage, fault restriction and fault scaling, *J. Struct. Geol.*, 24(9), 1413–1429, doi:10.1016/S0191-8141(01)00154-7.
- Wojtal, S. F. (1994), Fault scaling laws and the temporal evolution of fault systems, *J. Struct. Geol.*, 16(4), 603–612, doi:10.1016/0191-8141(94)90100-7.
- Wolf, R. A., K. A. Farley, and D. M. Kass (1998), Modeling of the temperature sensitivity of the apatite (U-Th)/He thermochronometer, *Chem. Geol.*, 148(1-2), 105–114, doi:10.1016/S0009-2541(98)00024-2.
- Wylde, S. J. (1996), Early Jurassic deformation in the Pine Forest Range, northwest Nevada, and implications for Cordilleran tectonics, *Tectonics*, 15, 566–583, doi:10.1029/95TC03693.